Twisted quantum interference in photoelectron holography with elliptically polarized fields

G. Kim [1,2,*] C. Hofmann [1,†] A. S. Maxwell,[3,1,‡] and C. Figueira de Morisson Faria[1,§]

[1]*Department of Physics and Astronomy, University College London, Gower Street, London WC1E 6BT, United Kingdom*

[2]*Department of Physics and Astronomy, Seoul National University, Seoul 08826, Republic of Korea*

[3]*Department of Physics and Astronomy, Aarhus University, 8000 Aarhus C, Denmark*

(Received 18 July 2022; accepted 30 September 2022; published 21 October 2022)

We perform a systematic analysis of how ultrafast photoelectron holography is influenced by an elliptically polarized field, with emphasis on quantum interference effects. We find that the interplay of the external field and the binding potential leads to twisted holographic patterns for low ellipticities and recover well-known angular offsets for high ellipticities. Using the Coulomb quantum-orbit strong-field approximation, we assess how the field ellipticity affects specific holographic patterns, such as the fan and the spider. The interplay of the external field and the binding potential leads to twisted holographic patterns in the fan and to loss of contrast in the spider. This behavior can be traced back to interfering electron trajectories and unequal changes in tunneling probability due to nonvanishing ellipticity. We also derive tunneling times analytically using the strong-field approximation, provide estimates for ellipticity ranges for which interference is expected to be prominent, and discuss how to construct continuous electron momentum distributions exploring the rotation symmetry around the origin.

DOI: 10.1103/PhysRevA.106.043112

I. INTRODUCTION

When matter interacts with a laser field whose intensity is of the order of 10^{14} W/cm^2, valence electrons can absorb more photons than necessary for ionization. This phenomenon is called above-threshold ionization (ATI) [1] and has been researched intensely in theory and applications [2,3]. It is explained by a physical picture of an electron being released through strong-field quantum tunneling or multiphoton ionization, accelerated by the field in the continuum, and finally captured by the detector [4]. Since it propagates to the detector via many possible pathways after ionization, an interference pattern is present in the photoelectron momentum distribution (PMD). These interference patterns are related to a wealth of information, such as the molecular structure and orbital geometries, essential for ultrafast imaging [5–9]. This has led to the inception of photoelectron holography [10–12], in which phase differences between distinct electron pathways lead to several types of structures (for a review see [13]). Photoelectron holography has been widely explored in linearly polarized fields, although there are studies in orthogonally polarized two-color [14–17] or elliptical fields [16,18].

In particular, tailored fields are a powerful tool for controlling both electron ionization and continuum propagation and thus phenomena such as ATI (for reviews see [3,19,20]). Complicated electron dynamics induced by a tailored field provide intricate interference patterns that could be used for revealing detailed internal orbital structures or focusing on specific electronic wave-function evolution paths. Various tailored fields, such as orthogonal two-color fields [14–17,21–28], bicircular fields [29–44], parallel two-color fields [45–51], and elliptically polarized fields (see, for example, [52–56]), have been studied extensively. In particular, ATI with elliptically polarized fields has been widely investigated in circular streaking approaches, using the numerical solution of the time-dependent Schrödinger equation (TDSE) [57–60], classical orbit theories [4,61–63], the strong-field approximation (SFA) [64], and the Coulomb eikonal approximation [65]. These studies considered, and sometimes even required, the field to be almost circularly polarized. In contrast, the low-ellipticity regime is comparatively less studied. Thereby, a key question is how to disentangle and interpret the holographic patterns that appear in the photoelectron spectra in terms of interfering electron orbits. This information is difficult to extract using the TDSE, in which specific quantum pathways cannot be switched on and off as one wishes. Furthermore, in its standard form, the SFA does not include the residual Coulomb potential in the electron's continuum propagation (for reviews see, e.g., [66,67]). This potential will influence ionization, continuum propagation, and consequently the shapes of the photoelectron momentum distributions.

Substantial progress in this direction has been made using the Coulomb quantum-orbit strong-field approximation (CQSFA) for linearly polarized fields [13]. The CQSFA has allowed explicit investigation into how holographic patterns form, through the isolation of interfering pairs of orbits. This includes the fan-shaped pattern close to the ionization threshold [68–70], spiderlike fringes along and near the field-polarization axis [10,11,71–73], and a spiral-like structure recently identified in experiments [74,75]. Multipath interference [76] and phase differences that can be used to probe orbital parity [77] have also been explored in conjunction

*gyeonghun.kim.phys@gmail.com
†c.hofmann@ucl.ac.uk
‡andrew.maxwell@phys.au.dk
§c.faria@ucl.ac.uk

with experiments. The CQSFA, however, has not yet been applied to fields with elliptical or circular polarization. As it is a nonadiabatic, fully Coulomb-distorted orbit-based method, the CQSFA is a powerful tool to assess photoelectron holography in this context.

Therefore, in this work we perform an analysis on the effect of the Coulomb potential in ATI with an elliptically polarized field based on quantum-orbit methods. We provide the fully analytic form of the SFA solutions with an elliptically polarized field and classify the orbits based on these solutions. Subsequently, we focus on the low-ellipticity regime, with emphasis on photoelectron holography. We show that the field ellipticity, together with the residual potential, modifies holographic structures, leading to changes in contrast or twisted spiral-like interference patterns. These features can be traced back to the quantum interference of specific pairs of orbits, which are affected in different ways. In the high-ellipticity regime, we recover the angular offsets known from previous angular streaking studies [58,62,63].

This paper is organized as follows. Section II offers an overview of the theoretical background upon which the work presented in this paper is based. Section III introduces saddle-point solutions for the ionization times, the formal extension of the CQSFA method for arbitrary ellipticity, and estimates for the maxima of the distributions and the ellipticity range for which interference is prominent. Subsequently, in Sec. IV we present the photoelectron momentum distributions computed for several field ellipticities, which are analyzed in terms of interfering electron trajectories. Finally, in Sec. V we state the main conclusions to be drawn from this work. We use atomic units throughout, unless otherwise stated.

II. BACKGROUND

The Hamiltonian H in strong-field ionization can be split into the atomic Hamiltonian H_a and the interaction Hamiltonian H_I as $H = H_a + H_I$, where

$$H_a = \frac{\hat{\mathbf{p}}^2}{2} + V(r) \tag{1}$$

is the atomic Hamiltonian. The interaction with the field is given by

$$H_I(t) = -\hat{\mathbf{r}} \cdot \mathbf{E}(t) \tag{2}$$

in the length gauge and assuming the dipole approximation [78]. The parameters used in this article are for helium, which is a widely used target in attosecond angular streaking studies (see, e.g., the reviews in [79,80]), although we work within the single-active-electron approximation. Theoretical models using effective single-active-electron potentials have been widely employed to describe attoclock experiments and are able to highlight their main features successfully. Further studies show that multielectron effects only play a secondary role in this context [81,82].

For the CQSFA methods, we consider the binding potential to be

$$V(r) = -\frac{1}{\sqrt{\hat{\mathbf{r}} \cdot \hat{\mathbf{r}}}}, \tag{3}$$

which can be used to describe helium in a single-active-electron computation asymptotically. In our SFA and CQSFA computations we choose the ionization potential $I_p = 0.97$ a.u. to be that of helium.

The semianalytic results are compared against a one-electron TDSE computation performed with the freely available software Qprop [83] using the pseudopotential

$$V_T(r) = -\frac{1 + (\alpha_1 e^{-\alpha_2 r} + \alpha_3 r e^{-\alpha_4 r} + \alpha_5 e^{-\alpha_6 r})}{r} f(r, r_0), \tag{4}$$

with $\alpha_1 = 1.231$, $\alpha_2 = 0.662$, $\alpha_3 = -1.325$, $\alpha_4 = 1.236$, $\alpha_5 = -0.231$, and $\alpha_6 = 0.480$ [84]. This potential is constructed such that its ground-state energy matches that of helium in a single-active-electron framework. Unless otherwise stated, $f(r, r_0) = 1$ throughout so that the binding potential is of Coulomb type and agrees with Eq. (3) asymptotically. However, in Fig. 3 we consider it to be of the form

$$f(r, r_0) = \begin{cases} 1 & \text{for } r < r_0 \\ \cos^7\left(\pi \frac{r - r_0}{2(L - r_0)}\right) & \text{for } r_0 \leqslant r < L \\ 0 & \text{for } r \geqslant L, \end{cases} \tag{5}$$

truncating the Coulomb potential smoothly starting at r_0 and leaving only the Coulomb-free laser potential outside L. In the present work the distance r_0 is chosen as a multiple m of the radius defined by the estimated tunnel exit $I_p/E_{\max}$ [85], which is the coordinate at which the electron reaches the continuum by tunneling through the potential barrier, while L is chosen as r_0 plus half an excursion amplitude. Explicitly, these parameters read

$$r_0 = m \frac{I_p}{E_{\max}} \tag{6}$$

and

$$L = r_0 + \frac{E_{\max}}{2\omega^2}, \tag{7}$$

where $E_{\max}$ is the field amplitude and relates to the ponderomotive energy U_p, field ellipticity ϵ, and frequency ω as $E_{\max} = \frac{2\omega\sqrt{U_p}}{\sqrt{1+\epsilon^2}}$.

The physical reason for using this kind of potential, where the truncation starts beyond the tunnel exit, is to alter the Coulomb tail, but not the potential barrier. This allows us to keep the tunneling process and the subbarrier dynamics unaltered, but change the continuum propagation. One-dimensional counterparts have been used by us in [86] to investigate resonant enhancements in high-order harmonic generation and in [87] to highlight the nonlocality of Bohmian trajectories using time-frequency analysis. Using more conventional short-range potentials would have influenced the tunneling dynamics, whose study is outside the scope of the present paper (see, e.g., [58,60]).

From the Schrödinger equation with the Hamiltonian above, we can calculate the transition amplitude of an electron from the bound state $|\psi_0\rangle$ to a final continuum state $|\psi_{\mathbf{p}}\rangle$ with momentum $\mathbf{p}$. The transition amplitude is defined as

$$M(\mathbf{p}) = -i \lim_{t \to \infty} \int_{-\infty}^{t} dt' \langle \psi_{\mathbf{p}}(t) | U(t, t') H_I(t') e^{iI_p t'} | \psi_0 \rangle, \tag{8}$$

where I_p is the ionization potential and $U(t,t')$ is the time-evolution operator associated with the full Hamiltonian $H_a + H_I(t)$. This integral equation is a general formal solution and a good starting point for developing quantum-orbit-based approaches. Throughout, we assume that the initial state $|\psi_0\rangle$ is the ground state $1s$ of helium.

A. Strong-field approximation

The strong-field approximation is a useful and often applied way to evaluate (8) analytically. The SFA consists in approximating the continuum by field-dressed plane waves and in neglecting the influence of the external laser field when the electron is bound, although continuum-to-continuum contributions may be incorporated perturbatively (for a recent review see [67]). In its standard form, it also neglects bound-to-bound transitions and considers only the ground state and the continuum, although one may also modify it to incorporate excitation [88,89].

In the SFA computations performed in this work, we will focus on the direct electrons, which reach the detector after tunnel ionization without further interacting with the core. This approximation corresponds to replacing the full time-evolution operator $U(t,t')$ by the Volkov time-evolution operator $U^{(V)}(t,t')$ in Eq. (8). This is also known as the Keldysh-Faisal-Reiss approximation [90–92]; for the specific formulation used here see also [93]. Then the semiclassical action corresponding to the propagation after tunnel ionization time t' can be calculated analytically as

$$S(\mathbf{p},t') = -\tfrac{1}{2}\int_{t'}^{\infty} [\mathbf{p}+\mathbf{A}(\tau)]^2 d\tau + I_p t'. \tag{9}$$

Here I_p is the ionization potential and $\mathbf{A}$ denotes the vector potential. The SFA transition amplitude may be associated with the coherent superposition of electron orbits in the continuum using saddle-point methods. Therefore, we seek values of t' for which Eq. (9) is stationary. This gives the saddle-point equation

$$\frac{\partial S(t')}{\partial t'} = \frac{[\mathbf{p}+\mathbf{A}(t')]^2}{2} + I_p = 0 \tag{10}$$

and (8) can be approximated by the coherent sum of orbits

$$M(\mathbf{p}) \sim \sum_s \mathcal{C}(t_s') e^{iS(\mathbf{p},t_s')}, \tag{11}$$

where the prefactor $\mathcal{C}(t_s')$ is given as

$$\mathcal{C}(t_s') = \sqrt{\frac{2\pi i}{\partial^2 S(\mathbf{p},t_s')/\partial t_s'^2}}\,\langle \mathbf{p}+\mathbf{A}(t_s')|H_I(t_s')|\psi_0\rangle \tag{12}$$

and t_s' are the saddle-point solutions. Since more than one orbit is related to a single final momentum, interference patterns will appear in the photoelectron momentum distributions. Due to the residual binding potential being neglected in the continuum propagation, the momentum $\mathbf{p}$ is conserved throughout.

B. Coulomb quantum-orbit strong-field approximation

The Coulomb quantum-orbit strong-field approximation also starts from Eq. (8), but instead of approximating the full time-evolution operator by its Volkov counterpart, time-slicing techniques and path-integral methods are used. Correspondingly, the Coulomb potential and the external field are treated on equal footing. We use the CQSFA action integrated over a two-pronged contour, first along the imaginary-time axis from t' to its real part and subsequently along the real-time axis from $\mathrm{Re}(t')$ up to $t \to \infty$ [94], and make the further approximation that the orbits are real in the continuum. A full treatment requires complex coordinates throughout and will lead to branch cuts; it has been discussed in [95]. Within the CQSFA, the Coulomb-distorted transition amplitude within the saddle-point approximation reads

$$M(\mathbf{p}_f) \propto -i \lim_{t\to\infty} \sum_s \left\{ \det\left[\frac{\partial \mathbf{p}_s(t)}{\partial \mathbf{r}_s(t_s')}\right]\right\}^{-1/2} \times \mathcal{C}(t_s') e^{iS(\mathbf{p}_s,\mathbf{r}_s,t,t_s')}, \tag{13}$$

where the semiclassical action is given by

$$S(\mathbf{p},\mathbf{r},t,t') = I_p t' - \int_{t'}^{t} [\dot{\mathbf{p}}(\tau)\cdot\mathbf{r}(\tau) + H(\mathbf{r}(\tau),\mathbf{p}(\tau),\tau)]d\tau. \tag{14}$$

The full Hamiltonian reads

$$H(\mathbf{r}(\tau),\mathbf{p}(\tau),\tau) = \tfrac{1}{2}[\mathbf{p}(\tau)+\mathbf{A}(\tau)]^2 + V(\mathbf{r}(\tau)). \tag{15}$$

The variables t_s', $\mathbf{p}_s$, and $\mathbf{r}_s$ are the solutions of the saddle-point equations

$$[\mathbf{p}(t')+\mathbf{A}(t')]^2 = -2I_p, \tag{16}$$

$$\dot{\mathbf{r}}(\tau) = \mathbf{p}(\tau) + \mathbf{A}(\tau), \tag{17}$$

$$\dot{\mathbf{p}}(\tau) = -\nabla_r V(\mathbf{r}(\tau)) \tag{18}$$

for energy conservation at tunnel ionization and the electron's intermediate momentum and position, respectively. One should note that, in Eq. (16), an additional approximation was made, namely, that the momentum in the first part of the contour is constant and equal to $\mathbf{p}_0 = \mathbf{p}(t')$, and that, in contrast to the SFA transition amplitude, one must take into consideration the intermediate variables $\mathbf{r}(\tau)$ and $\mathbf{p}(\tau)$, $t' < \tau < t$, in the continuum propagation equations (17) and (18). The momentum at the detector is $\mathbf{p}(t) = \mathbf{p}_f$. The term $\mathcal{C}(t_s')$ is given by Eq. (12), but with $\mathbf{p}$ replaced by the initial momentum $\mathbf{p}_0$. For details about the CQSFA, refer to [94,96].

In the present work we consider ionization times within up to four cycles and the continuum propagation extends to roughly 20 cycles of the field. Since the laser field is periodic and no pulse envelope is considered in the CQSFA method, restricting ionization times to a single cycle leads to some ambiguity with regard to where the cycle starts and finishes. This ambiguity will influence the intracycle interference patterns and could be removed by considering distributions incoherently averaged over the offset phases marking the start of these unit cells, but this method will not be employed here. For details see [76].

III. ANALYTICAL ESTIMATES AND IONIZATION TIMES

In the following we consider an elliptically polarized field approximated by two orthogonally polarized monochromatic waves of frequency ω. This approximation holds for long enough pulses. The vector potential and corresponding elec-

tric field are given by

$$\mathbf{A}(t) = \frac{2\sqrt{U_p}}{\sqrt{1+\epsilon^2}}[\cos(\omega t)\hat{\mathbf{e}}_z + \epsilon\sin(\omega t)\hat{\mathbf{e}}_x],$$
$$\mathbf{E}(t) = \frac{2\omega\sqrt{U_p}}{\sqrt{1+\epsilon^2}}[\sin(\omega t)\hat{\mathbf{e}}_z - \epsilon\cos(\omega t)\hat{\mathbf{e}}_x], \quad (19)$$

where ϵ is the field ellipticity and $\hat{\mathbf{e}}_z$ and $\hat{\mathbf{e}}_x$ are the unit vectors along the major and minor polarization axes, chosen as $\hat{z}$ and $\hat{x}$, respectively. We keep the ponderomotive energy U_p constant for varying ellipticity. Equation (19) implicitly states that we define a unit cell starting at a phase $\phi = 0$. Other unit cells could be chosen by setting $\omega t \to \omega t + \phi$, where ϕ is an offset phase used to define the beginning of the unit cell. For a coherent sum of ionization times over many cycles, this will not play a role, but for a single-cycle photoelectron momentum distribution this will lead to some ambiguity in the patterns [76]. Both the CQSFA and SFA are solved in the polarization plane $p_z p_x$, which qualitatively describes the dynamics we are interested in. Quantitatively, however, there will be differences in the positions and strengths of the fringes in these two-dimensional models and the three-dimensional calculation of the TDSE we are employing, including due to electron trajectories crossing focal points leading to Gouy phase shifts. This effect has been discussed in [97] for fields with linear polarization, but it is a general property of scattering trajectories. Furthermore, CQSFA and SFA calculations use a monochromatic field while the TDSE requires a pulse envelope, resulting in a larger spectral width, and the effective binding potentials are different close to the core. Consequently, we expect the agreement between the methods employed here to be only of qualitative nature.

Next we will use the action associated with the direct SFA transition amplitude to provide analytic estimates for the centers of the electron momentum distributions, as well as the parameter range for which quantum interference is expected to be significant. We will also employ the tunnel ionization equation (10) to derive analytic solutions for the ionization times. Although such estimates are approximate in the presence of residual potentials, they give valuable insight and can also be used as initial guesses for the CQSFA.

The SFA action for the elliptically polarized fields (19) reads

$$S_d(\mathbf{p}, t') = \left(\frac{p_z^2 + p_x^2}{2} + I_p + U_p\right)t' + \frac{U_p}{2\omega(1+\epsilon^2)}[\sin 2\omega t' - \epsilon^2 \sin 2(\omega t')] + \frac{2\sqrt{U_p}}{\omega\sqrt{1+\epsilon^2}}[p_z \sin\omega t' - \epsilon p_x \cos(\omega t')], \quad (20)$$

where $\mathbf{p} = (p_z, p_x)$. The corresponding tunnel ionization equation (10) then reads

$$\left(p_z + \frac{2\sqrt{U_p}}{\sqrt{1+\epsilon^2}}\cos(\omega t')\right)^2 + \left(p_x + \frac{2\epsilon\sqrt{U_p}}{\sqrt{1+\epsilon^2}}\sin(\omega t')\right)^2 + 2I_p = 0. \quad (21)$$

Equation (21) is a superposition of circles of complex radii centered at

$$(p_z^{(c)}(t'), p_x^{(c)}(t')) = \left(-\frac{2\sqrt{U_p}}{\sqrt{(1+\epsilon^2)}}\cos\omega t', -\epsilon\frac{2\sqrt{U_p}}{\sqrt{(1+\epsilon^2)}}\sin\omega t'\right), \quad (22)$$

which can be used to estimate the maxima of the distributions and the region for which quantum interference is significant.

A. Widths and maxima of the distributions

The preceding section dealt with the centers of momentum distributions (or most probable final photoelectron momenta). However, in order to see interference patterns in the PMD we must consider the widths of photoelectron wave packets and whether or not they overlap. Here we provide estimates for the ellipticity range for which prominent intracycle interference patterns are expected. The estimates below assume that ionization is most probable at the peak of the field, which lies along the z axis, and is valid for small or medium ellipticities. They have also been performed within the SFA, for which the field-dressed momentum is conserved in the continuum. For linear and elliptical polarization, $p_z^{(c)} = 0$ is expected since $\omega t' = (2n+1)\pi/2$ are the peaks in the electric field $\mathbf{E}(t')$, which points along the major axis and $A_z(t') = 0$ for those specific times [see Eqs. (19) and (22)]

$$(p_z^{(c)}, p_x^{(c)}) = \left(0, -\epsilon\frac{2\sqrt{U_p}}{\sqrt{1+\epsilon^2}}(-1)^n\right). \quad (23)$$

For events displaced by half a cycle, $p_x^{(c)}$ will always have opposite signs, so the distance between the center of the distributions yields

$$p_{x1}^{(c)} - p_{x2}^{(c)} = \epsilon\frac{4\sqrt{U_p}}{\sqrt{1+\epsilon^2}}. \quad (24)$$

In this work we are investigating interference patterns and hence require wave packets ionized at opposite half cycles to still overlap to some degree in the final momentum distribution. We can find an estimate of the interference width, starting from Delone and co-workers' [98,99] description of the width of the wave packets approximated to Gaussian shapes

$$\sigma_\perp = \sqrt{\frac{\omega\sqrt{U_p}}{\sqrt{1+\epsilon^2}\sqrt{2I_p}}}. \quad (25)$$

Requiring that the two centers are a maximum of $5\sigma_\perp$ apart from each other such that there is still a significant enough overlap between them to show interference patterns originating from different half cycle orbits, we find

$$p_{x1}^{(c)} - p_{x2}^{(c)} = 5\sigma_\perp,$$

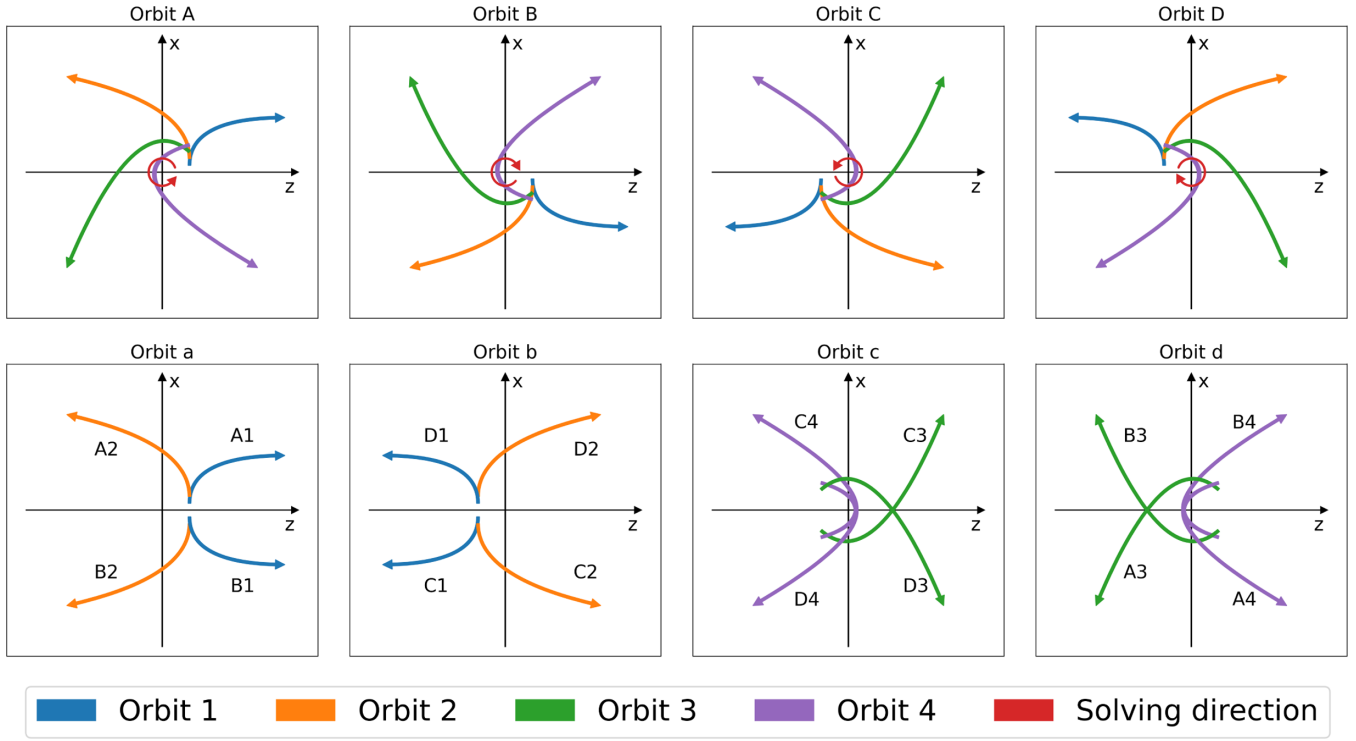

FIG. 1. Schematic representation of the classification of orbits used in this paper. The colors of the orbits give orbits 1–4, according to the classification criteria introduced in [96,103] of the CQSFA with a linearly polarized field. Orbits A and B (C and D) correspond to the times $t_{1,n}$ ($t_{2,n}$) in Eq. (29), solved asymptotically in the counterclockwise and clockwise directions, which are marked as red circular arrows. Classification of orbits a–d are used for calculating PMDs. The curves indicated in the figure are not actual electron trajectories but schematic illustrations of the orbit's overall behavior.

$$\epsilon \frac{4\sqrt{U_p}}{\sqrt{1+\epsilon^2}} = 5\sqrt{\frac{\omega\sqrt{U_p}}{\sqrt{1+\epsilon^2}\sqrt{2I_p}}}. \tag{26}$$

Although somewhat arbitrary, this limiting shift of $5\sigma_\perp$ has been chosen as an educated guess, by assuming that an overlap of at least $1\sigma_\perp$ may occur within a $3\sigma_\perp$ range from each of the peaks such that some interference pattern is still visible (on a logarithmic scale such as presented in Fig. 2). Solving for ϵ yields

$$\epsilon_c = \frac{5\sqrt{\omega}}{32\sqrt{I_p}\sqrt{U_p}}\sqrt{5^2\omega + \sqrt{2048 I_p U_p + 5^4\omega^2}}, \tag{27}$$

an estimate for a critical value of ellipticity, beyond which interferences are expected to vanish. We can further justify the choice of 5σ by performing the derivation of the equation for ϵ_c for arbitrary $s\sigma_\perp$ distance between the two centers

$$\epsilon_c(s) = \frac{s\sqrt{\omega}}{32\sqrt{I_p}\sqrt{U_p}}\sqrt{s^2\omega + \sqrt{2048 I_p U_p + s^4\omega^2}}. \tag{28}$$

Evaluating the above equation with the same laser parameters but for $s = 4$, we find $\epsilon(4) = 0.26$, while for $s = 6$ it predicts $\epsilon_c(6) = 0.4$, and in general the scaling behaves as $\epsilon_c(s) = 0.333\,924 + 0.070\,311\,7(s-5) + O((s-5)^2)$. The choice of $s = 5$ is appropriate for our calculations and gives us an idea of how the range of ellipticity with intercycle interference depends on various laser parameters such as the frequency. However, we also expect that in different circumstances (for example, depending on the signal-to-noise ratio of particular experiments) this s parameter would have to be adapted.

Equation (27) scales proportionally to $\sqrt{\omega} + O(\sqrt{\omega}^3)$ for constant ponderomotive energy U_p and all other parameters. This scaling is consistent with the parameter range employed in this work. Evaluating (28) for the laser parameters typically used in our study (see, for example, Fig. 2), we find a critical value of around $\epsilon_c = 0.33$, comparable to the results of our calculations in that same figure.

B. SFA ionization times

With the elliptically polarized field as given in Eq. (19), we obtain the analytic form of the ionization time by solving the SFA saddle-point equation (10) for tunnel ionization in the whole $p_z p_x$ plane. This goes beyond the work in [100], which proved that the ionization time with elliptically polarized fields has two solutions, but only provided analytic expressions along the major polarization axis. In the present paper we calculate the ionization times analytically and determine the regions in the momentum plane for which they are valid.

Since the ionization times' analytic form is complicated, we introduce $t_{11,n}$, $t_{12,n}$, $t_{21,n}$, and $t_{22,n}$ in Eq. (29), where n denotes the cycle number and the variables ζ and η are defined in Appendix A. These expressions are the candidates for the ionization time. The solutions $t_{11,n}$ and $t_{21,n}$ are both valid in the first and third quadrants in the momentum plane and $t_{12,n}$ and $t_{22,n}$ both hold in the second and fourth quadrants.

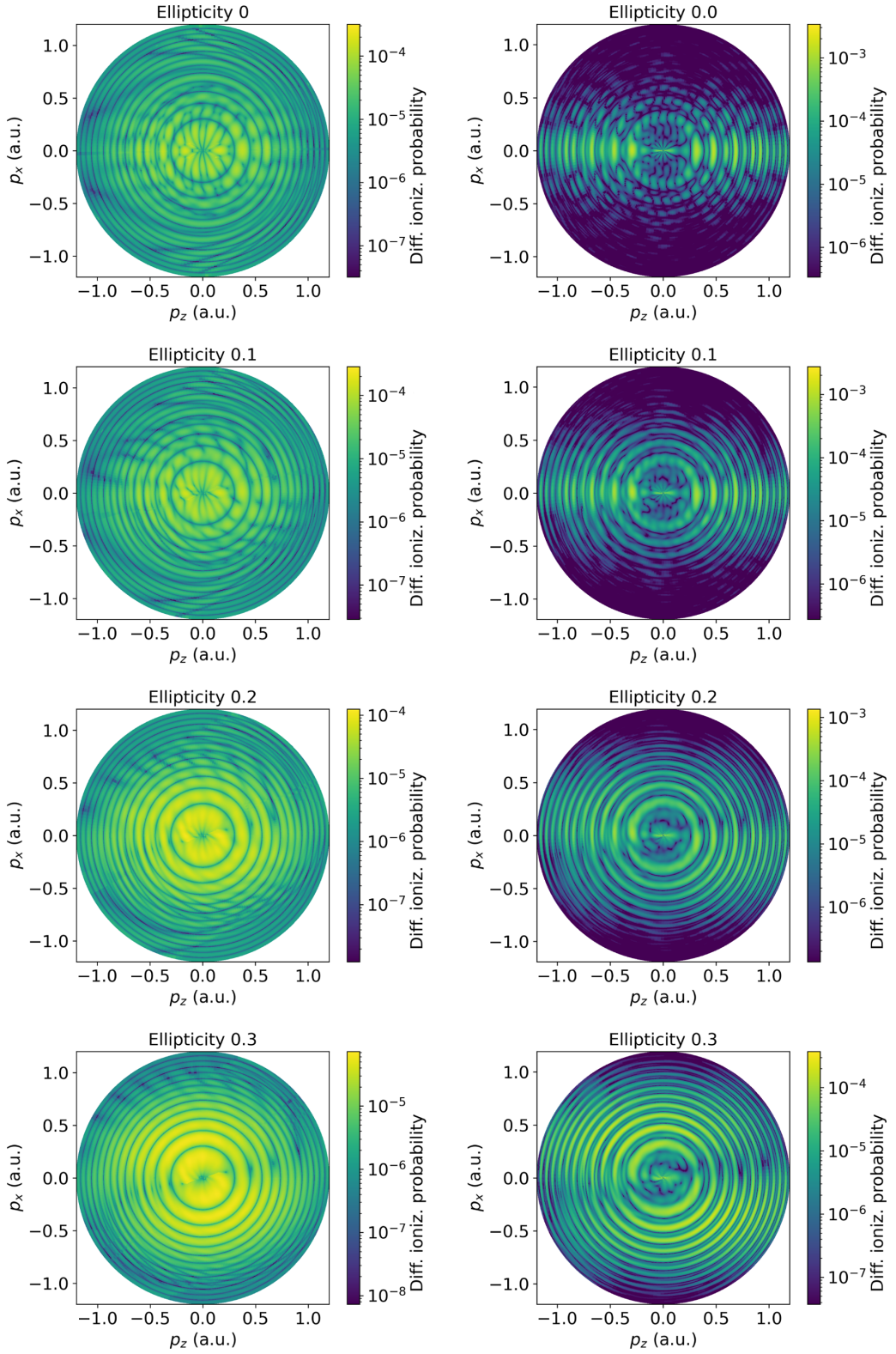

FIG. 2. Photoelectron momentum distributions calculated for helium in a field of intensity 2.5×10^{14} W/cm^2 and wavelength $\lambda = 735$ nm, whose ellipticity increases from $\epsilon = 0$ to $\epsilon = 0.3$. The left and the right columns have been calculated with the CQSFA and the Schrödinger equation solver Qprop [83], respectively. For Qprop, we have used an envelope with a $1 - \cos^{16}$ shape for a pulse with a total duration of four cycles, creating a near-flattop pulse, and the final PMDs have been calculated with the i-SURFV option [83]. Each panel has been normalized to its maximum value and plotted in logarithmic scale.

We group $t_{11,n}, t_{12,n}$ and $t_{21,n}, t_{22,n}$ as $t_{1,n}$ and $t_{2,n}$ to render a solution valid in the full $p_z p_x$ plane [Eq. (29)]. We will refer to the ionization quantum trajectory associated with the ionization time $t_{1,n}$ as an orbit a and one with $t_{2,n}$ as an orbit b (see Sec. III C for more details on orbit classification). The necessity of specifying domains in the $p_z p_x$ plane stems from the fact that Eq. (29) is obtained from a quartic equation. This implies that two solutions become spurious in specific domains. This derivation is sketched in Appendix A:

$$
\begin{aligned}
t_{11,n} &= \frac{2\pi(n+1)}{\omega} - \frac{1}{\omega}\arccos\left[\frac{-p_z+\zeta+i\sqrt{(1-\epsilon^2)(2I_p+p_x^2)+\epsilon^2 p_z^2+4\zeta^2+\eta}}{2(1-\epsilon^2)\sqrt{U_p}}\right],\\
t_{12,n} &= \frac{2\pi(n+1)}{\omega} - \frac{1}{\omega}\arccos\left[\frac{-p_z-\zeta+i\sqrt{(1-\epsilon^2)(2I_p+p_x^2)+\epsilon^2 p_z^2+4\zeta^2-\eta}}{2(1-\epsilon^2)\sqrt{U_p}}\right],\\
t_{21,n} &= \frac{2\pi(n)}{\omega} + \frac{1}{\omega}\arccos\left[\frac{-p_z+\zeta-i\sqrt{(1-\epsilon^2)(2I_p+p_x^2)+\epsilon^2 p_z^2+4\zeta^2+\eta}}{2(1-\epsilon^2)\sqrt{U_p}}\right],\\
t_{22,n} &= \frac{2\pi(n)}{\omega} + \frac{1}{\omega}\arccos\left[\frac{-p_z-\zeta-i\sqrt{(1-\epsilon^2)(2I_p+p_x^2)+\epsilon^2 p_z^2+4\zeta^2-\eta}}{2(1-\epsilon^2)\sqrt{U_p}}\right],
\end{aligned}
\tag{29}
$$

$$
\begin{aligned}
t_{1,n} &= \begin{cases} t_{11,n} & \text{if } p_z p_x \geqslant 0 \\ t_{12,n} & \text{if } p_z p_x < 0, \end{cases}\\
t_{2,n} &= \begin{cases} t_{21,n} & \text{if } p_z p_x \geqslant 0 \\ t_{22,n} & \text{if } p_z p_x < 0. \end{cases}
\end{aligned}
\tag{30}
$$

Further to that, the two orbits given by the times in (29) are not always physically significant. Depending on the parameter range, one of the saddle-point solutions may become inaccurate and lead to divergencies in the PMDs. This is due to the presence of Stokes transitions, which are directly related to topological changes in the contours introduced by nonzero ellipticity. For high ellipticities, a single ionization time will be associated with a specific final momentum or angle. This behavior makes the attosecond angular streaking method, the attoclock, possible [101,102]. These Stokes transitions were first identified in [64] for a restricted parameter range and in [100] it was stressed that for elliptically polarized fields there is *always* a Stokes transition. However, for low ellipticity they are outside the physically relevant parameter range. Details about Stokes transitions and the high ellipticity limit for $\mathrm{Re}(t')$ are provided in Appendixes B and C, respectively.

C. CQSFA ionization times and orbit classification

In contrast to the SFA, the saddle-point solutions for the CQSFA cannot be directly expressed analytically; thus, we have to solve the saddle-point equations (16)–(18) numerically. Nevertheless, we can expect that the SFA and CQSFA solution dynamics are most similar in those orbits whose final momentum is the same as its ionization direction. Therefore, we can use the SFA solution as a first guess at some point in the momentum space. Then we can asymptotically solve other points by using a solved neighbor point as an initial guess. In this method, because of the core in the center, clockwise and counterclockwise solved solutions are different; therefore, we can obtain two CQSFA solutions from one SFA solution. As shown in Fig. 1, we named the counterclockwise (clockwise) solved solution derived from $t_{1,c}$ as solution class A (B) and that derived from $t_{2,c}$ as C (D).

Each solution class A–D contains a single orbit 1–4, whose criteria are its ionization direction and final momentum. This classification into orbits 1–4 is robust for the linearly polarized case because orbits in each classification A–D show similar dynamics. For linear polarization, orbit 1 reaches the detector directly, orbits 2 and 3 are field-dressed Kepler hyperbolae, and orbit 4 goes around the core. This classification was introduced in [103] and employed by us in previous publications (see, e.g., [94,96]) and one can understand how such orbits interfere by piecing them together. For instance, orbit $A1$ reaches the detector directly in the first quadrant of the figure and interferes with orbits $C3$ and $D2$, which both start on the "wrong" side half a cycle later, but differ in their transverse momentum behavior. Finally, orbit $B4$ starts on the same side as $A1$ (meaning it is born in the same half cycle), but goes around the core before eventually reaching the detector. The orbits in this example form interference patterns in the first quadrant of the momentum plane.

For an elliptically polarized field, on the other hand, the reflection symmetry about both major and minor polarization axes breaks down. Therefore, this symmetry breaking makes the PMD of each orbit with the classification employed in the linear case discontinuous in both the major and minor polarization axes. Instead, the final PMD typically shows a point symmetry about the origin. Therefore, we introduce a new generalized orbit classification a–d, according to the bottom panels in Fig. 1. Orbits whose tunnel exits are located at $z > 0$ ($z < 0$) and whose momentum components p_x do not change sign during continuum propagation are designated as a (b), while orbits c (d) start at $z < 0$ ($z > 0$) and switch half planes during continuum propagation. Note that this classification respects the fact that a nonvanishing field ellipticity introduces a preferential rotational direction, which must be taken into consideration. For clarity, in Table I we provide the correspondence between both labeling systems. For the first and fourth quadrants, the classifications 1–4 and a–d coincide, but this is not the case in the other two quadrants.

In this paper we will use this new heuristic classification for orbits a–d as outlined in Fig. 1 and specified in Table I.

TABLE I. Orbit classification compared to the linearly polarized case. In the CQSFA calculation with a linearly polarized field, the labeling 1–4 classifies the orbit with two different conditions, the sign of $z_0 p_{fz}$ and $p_{fx} p_{0z}$. However, with an elliptically polarized field, because of the broken reflection symmetry, orbits 1–4 could not directly be matched with orbits a–d. For convenience, we provide a relation between orbits 1–4 and a–d here. The first column gives the orbit classification 1–4 used in our previous work for linearly polarized fields, the second column provides the conditions upon the tunnel exit and momentum components for each orbit, and the remaining columns yield the classification a–d in each quadrant (quad.) of the $p_z p_x$ plane.

Orbit	$z_0 p_{fz}$	$p_{fx} p_{0z}$	1st quad.	2nd quad.	3rd quad.	4th quad.
1	+	+	a	b	b	a
2	−	+	b	a	a	b
3	−	−	c	d	d	c
4	+	−	d	c	c	d

Two main points considered in this classification are grouping the orbits with similar dynamical behaviors and minimizing discontinuity issues in the single-orbit PMDs. Since a and b are less affected by the Coulomb potential, their action is more similar to the SFA case than c and d. This difference is more conspicuous with higher ellipticity. However, it is impossible to create fully continuous PMDs only with orbits a and b (c and d). Most of the significant interference patterns appear near the minor polarization axis, not the major axis; we choose the classification which makes PMD continuous on the minor axis. Note that the method of classification does not affect the complete PMD calculation, whose outcome is displayed in Figs. 2 and 4.

IV. PHOTOELECTRON MOMENTUM DISTRIBUTIONS

Below we discuss photoelectron momentum distributions and provide interpretations for the features encountered in terms of the saddle-point solutions for the ionization time t'. Throughout, unless necessary, $\mathbf{p}$ refers to the *final* momentum, measured at the detector. Due to the presence of the Coulomb potential in the continuum, for the CQSFA and TDSE computations this will not be the momentum $\mathbf{p}_0$ at the instant of ionization. For the SFA, the final and initial momenta are identical.

A. Comparison of the CQSFA with other methods

We will start by comparing the photoelectron-momentum distributions calculated with the CQSFA with the outcome of other approaches, such as the full TDSE solution and the standard SFA. Figure 2 shows photoelectron-momentum distributions computed with the CQSFA and the one-electron time-dependent Schrödinger solver Qprop [83,104], for a range of driving-field ellipticities (left and right columns, respectively).

The PMDs exhibit ATI rings stemming from intercycle interference and, for vanishing and low ellipticity, holographic patterns resulting from interfering intracycle events. These patterns are clearly identifiable for linearly polarized fields (top row in Fig. 2), as the spiderlike fringes near the polarization axis ($\theta = 0$), a fan-shaped structure close to the ionization threshold, and a carpetlike structure around the angle $\theta = 90^\circ$. Besides minor issues associated with the finite pulse length, the patterns are symmetric with regard to reflections around $\theta = 0^\circ$ and 90°. For nonvanishing ellipticity, these symmetries are lost and the patterns start to twist in the counterclockwise direction, following the rotational sense of the driving field. Furthermore, the centers of the distributions start to split and the interference fringes become more and more blurred for increasing ellipticity. These features are observed throughout, although there are quantitative differences.

If one considers a binding potential such that its effective barrier remains the same but its tail is truncated by multiplying a smooth function $f(r, r_0)$ to the Coulomb potential as described in Eqs. (5) [86], the rotational shifts in the holographic

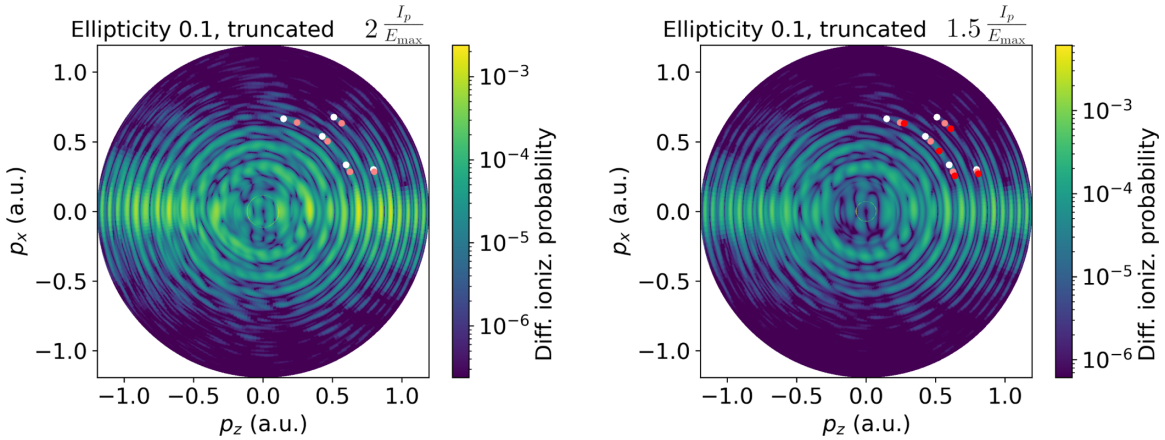

FIG. 3. Photoelectron momentum distributions calculated for helium in a field of ellipticity $\epsilon = 0.1$ and the same parameters as in Fig. 2 using the Schrödinger solver Qprop, but considering a truncated potential according to Eq. (5). We have used an envelope with a $1 - \cos^{16}$ shape for a pulse with a total duration of four cycles, creating a near-flattop pulse, and the final PMDs have been calculated with the i-SURFV option [83]. Each panel has been normalized to its maximum value and plotted in logarithmic scale. White dots represent selected interference maxima from the full Coulomb tail calculation, light red dots from truncation with $m = 2$, and dark red dots with $m = 1.5$; the shift between the dots highlights the rotation of the interference pattern.

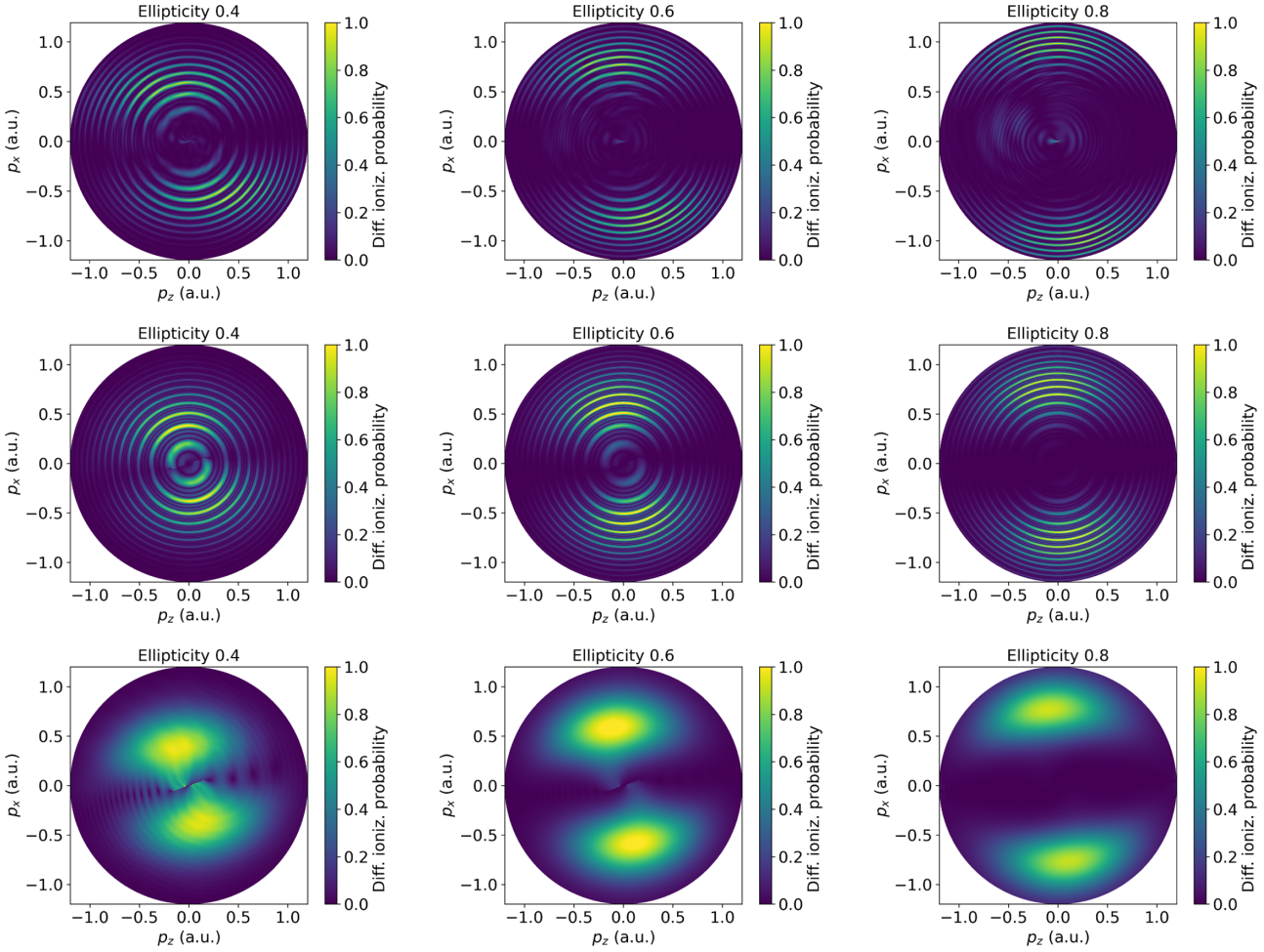

FIG. 4. Photoelectron momentum distributions computed for ellipticity values higher than that specified in Sec. III. For the Qprop calculation in the top row and the CQSFA results in the middle row, all other field and atomic parameters are the same as in Fig. 2. For the CQSFA in all cases, we have only employed orbits a and b as the remaining orbits are strongly suppressed in this ellipticity range [see the Appendixes and the discussion of $\mathrm{Im}(t')$]. The bottom row shows the single-cycle CQSFA result; thus no intercycle ATI rings are visible anymore. We have chosen to plot the PMDs in linear scale in order to facilitate the comparison with the existing literature and highlight the doubly peaked structure that exists in these distributions.

patterns are reduced. This is shown in Fig. 3, for which the potential started to be altered at $m = 2$ and 1.5 in Eq. (6), respectively, corresponding to r_0 being 2 or 1.5 times the approximate tunnel exit. The dots of different hues highlight the rotation of the interference pattern between different calculations. White dots highlight selected interference maxima in the calculation with the full Coulomb tail, included in Fig. 2. Light red dots highlight the position of those same interference maxima in the case of the Coulomb tail being truncated with $m = 2$ and dark red the same maxima again for the truncation even closer to the binding potential with $m = 1.5$.

Interestingly, the fan-shaped pattern near the ionization threshold is also considerably altered, which is expected due to it being caused by the Coulomb tail [94,105]. There is still some residual twisting, possibly associated with under-the-barrier dynamics.

The behavior described above is markedly different from that observed for high ellipticities, which we illustrate in Fig. 4. Both for the CQSFA and TDSE computations, the figure shows sickle-shaped distributions with an angular offset. This is the shape of the photoelectron distribution typically used in angular streaking attoclock measurements [60,63,106,107]. The holographic patterns have practically faded and the only visible interference patterns are the ATI rings, resulting from intercycle rather than intracycle interference. The rings are quite prominent in the top and middle row of Fig. 4, which were computed for four-cycle pulses. In order to highlight the shapes of the distributions and the angular offsets, in the bottom row we plot CQSFA results for a single cycle. The single-cycle distributions confirm that the intracycle patterns are either very faint (see the plot for ellipticity 0.4 on the left-hand side) or absent (see the remaining plots). For high ellipticity, the blurring of the holographic patterns is predominantly caused by a reduction in the number of interfering orbits, which coalesce close to Stokes transitions (see Appendix B and [100]). The PMDs obtained with the CQSFA exhibit maxima at lower momenta than those of

Qprop. This is likely to be due to the differences in dimensionality, pulse shapes, and binding potentials used (see Secs. II and III for details).

In Fig. 5 we perform a direct comparison of the CQSFA with the interference from the direct SFA pathways, within a single cycle. This facilitates the study of holographic intracycle interference due to the absence of ATI rings. By making these choices, the role of the Coulomb potential becomes even clearer, and the CQSFA plots show superimposed sets of twisted fringes in the counterclockwise direction for elliptical polarization. These fringes are more visible in the high-energy region, but are present in a broad range of momenta. Another noteworthy feature is that the spider loses its dominance around ellipticity $\epsilon = 0.2$ (left-hand side, second row from the bottom) and all patterns become increasingly blurred. For the largest ellipticity in the figure (left-hand side, bottom row), the PMD exhibits a typical splitting, with offset phase shifts due to the presence of the Coulomb potential.

This behavior is markedly different from that of the SFA PMDs, shown in the right column of Fig. 5, which display near vertical fringes and no angular offset. For increasing ellipticity, the PMDs in the SFA split, but the fringes remain roughly the same. The quantum interference fades around $\epsilon = 0.3$, in agreement with our estimates in Sec. III. Furthermore, for intermediate ellipticities, the CQSFA maxima are closer to the major polarization axis than the SFA estimates, which is evidence of Coulomb focusing.

B. Quantum-orbit analysis of holographic patterns

In Fig. 6 we analyze specific holographic structures by looking at how pairs of trajectories interfere. Here we employ the orbit classification in Sec. III, which keeps the distributions continuous along the minor axis. There may be, however, discontinuities along the major axis. Throughout this section, our analysis will focus on the low- and intermediate-ellipticity regimes, for which all orbits are present in the momentum regions of interest and the loss of contrast occurs mainly due to increasingly different ionization probabilities associated with the contributing orbits. This is a different scenario than that occurring for high ellipticities, for which orbits coalesce.

In the left column of Fig. 6 we see the PMDs resulting from the interference of orbits a and b. For linear polarization, they give rise to a fan-shaped structure near the ionization threshold, displayed in the top left corner of the figure. This is expected from our previous studies of holographic structures in linearly polarized fields [94,105]. Once the polarization increases, the fan starts to lose contrast until the interference pattern ultimately fades. The loss of contrast takes place away from the major polarization axis, with the peaks of the distributions moving further apart. This happens because the fan stems from interfering trajectories that start half a cycle apart, whose momentum component p_x parallel to the minor polarization axis does not change sign during the continuum propagation. Hence, the final momentum distributions resulting from such orbits will be peaked at opposite half planes and will overlap less and less as the ellipticity increases. The remainder of the fan occurs where the overlap is still significant.

This behavior is very distinct from that of the spider, which is shown in the middle column of Fig. 6 and results from the interference of orbits b and c. For linear polarization, the spider is located in the region of positive p_z. According to the classification in Fig. 1, it is formed by the interference of orbits $D2$ and $C3$ ($D3$ and $C2$) in the upper (lower) half plane starting in the same half cycle. The structure forming in the region of negative p_z also stems from the interference of orbits starting in the same half cycle, namely, $D1$ interfering with $C4$ and $C1$ interfering with $D4$, although it is not known as "the spider." For linear polarization, the spider is symmetric upon reflection with regard to the $p_z = 0$ axis. For nonvanishing ellipticity, this symmetry is lost, with the whole structure undergoing a counterclockwise rotation and becoming more prominent in the lower momentum half plane. There is also a blurring in the spider fringes, initially close to the major polarization axis (second and third rows) and subsequently throughout (bottom row).

Finally, in the right column of Fig. 6 we plot the PMDs resulting from the interference of orbits a and c. Those orbits start at different half cycles, but the final momenta will populate the same half plane. This is due to the momentum component p_x along the minor polarization axis changing sign during the electron's continuum propagation. With increasing ellipticity, the fringes start to exhibit blurring in the vicinity of the p_z axis or, by inspecting the upper half plane, close to the maximum associated with orbit a. Contrast is retained for higher values of p_x. There is also a difference in strength in the upper and lower half plane. By inspection, one can see that many twisted patterns in Figs. 2 and 5 in high photoelectron momentum regions can be attributed to the remnants of the spider and of the fringes associated with the interference of orbits a and c. A summary of how specific holographic structures behave with increasing ellipticity is provided in Table II.

Next we will have a closer look at the blurring that occurs for the spider and the patterns due to the interference of orbits a and b, among other effects. A loss of contrast may be due to changes in ionization probabilities, to orbit 3 being suppressed due to rescattering being hindered as the ellipticity increases, or to both effects.

The changes in the ionization probability can be inferred from the imaginary parts of the ionization times, as the ionization probabilities roughly scale as $\exp[-2\,\mathrm{Im}(t')]$. Hence, the larger $\mathrm{Im}(t')$ is, the more suppressed a specific orbit will be. In Fig. 7 we plot $\mathrm{Im}(t')$ along the minor polarization axis $p_z = 0$ for the ellipticities used in Fig. 6. Our analysis will focus on the CQSFA orbits, but, in the top panels of Fig. 7, we also provide $\mathrm{Im}(t')$ for the SFA orbits a and b. Figure 7 displays $\mathrm{Im}(t')$ as functions of the final and initial electron momentum component p_x along the minor polarization axis, that is, p_{fx} and p_{0x} (top and bottom rows, respectively). In order to cover a larger range for the initial momentum, in the bottom panels of Fig. 7 the orbits were selected such that all values of the parallel momenta are allowed. This is relevant as, strictly speaking, an electron cannot escape if $p_{0x} = p_{0z} = 0$ and will cause the divergencies discussed below.

For linearly polarized fields (left column in Fig. 7), $\mathrm{Im}(t')$ is symmetric with regard to the reflection $p_x \to -p_x$ for all orbits. This behavior mirrors that observed for the PMDs in Figs. 2, 5, and 6, which exhibit this symmetry for linear

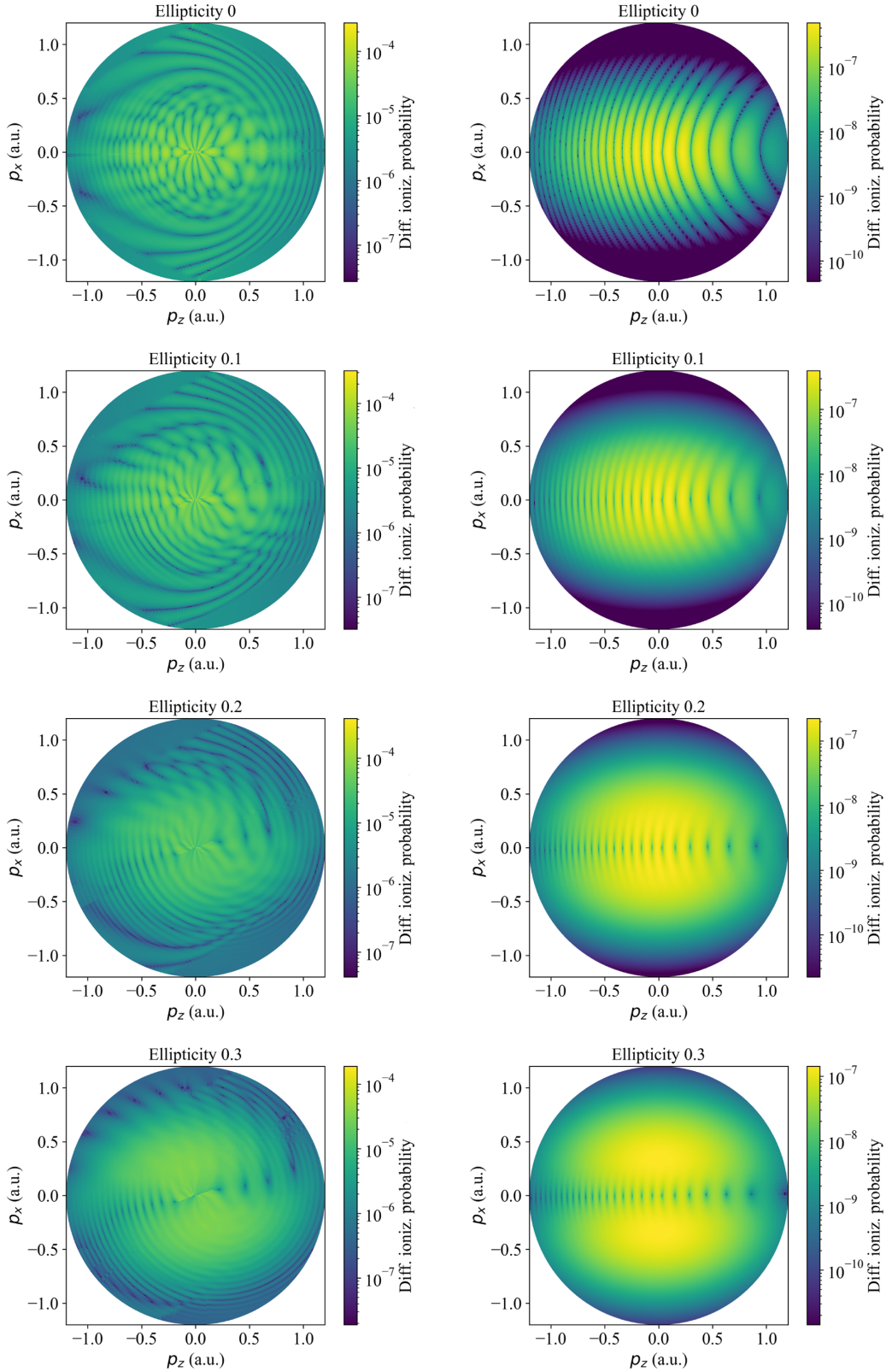

FIG. 5. Photoelectron momentum distributions calculated for helium in a field of intensity 2.5×10^{14} W/cm^2 and wavelength $\lambda = 735$ nm, whose ellipticity increases from $\epsilon = 0$ to $\epsilon = 0.3$, considering a single cycle and a unit cell with $\phi = 0$. The left and right panels display the outcome of the CQSFA and SFA, respectively. For the SFA, we have employed the direct orbits a and b, while for the CQSFA orbits a to d were included. All panels have been normalized to their maximum values and a logarithmic scale was used.

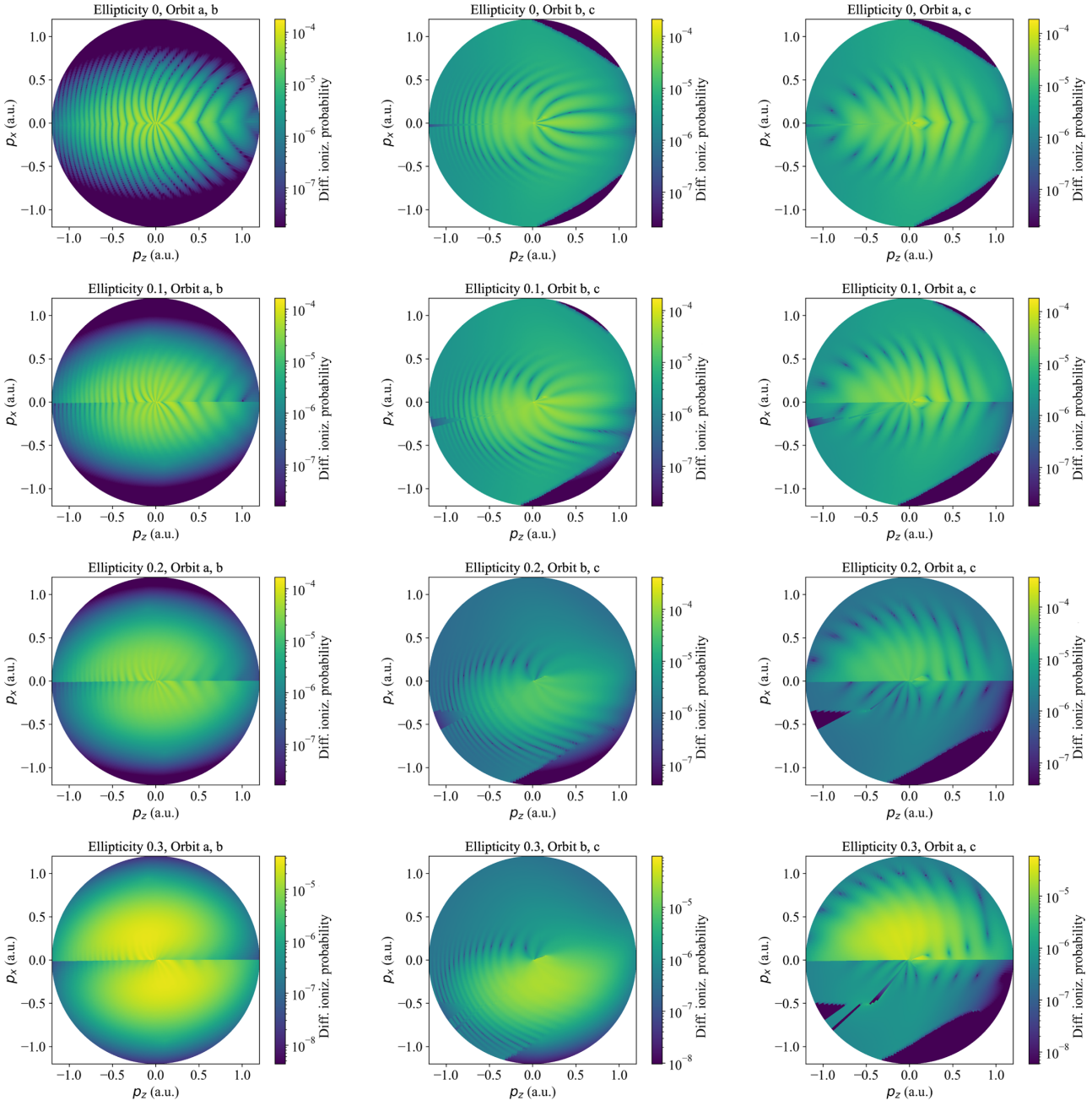

FIG. 6. Photoelectron momentum distributions calculated for helium in a field of intensity 2.5×10^{14} W/cm^2 and wavelength $\lambda = 735$ nm, whose ellipticity increases from $\epsilon = 0$ to $\epsilon = 0.3$, considering a single cycle and a unit cell with $\phi = 0$. The left column shows the interference between orbits a and b, the middle column orbits b and c, and the right column orbits a and c. The orbit characterization is provided in Sec. III C. All panels have been normalized to their maximum values and a logarithmic scale was employed.

polarization. For the CQSFA orbits a and b, Im(t') displays a behavior similar to its SFA counterparts, with a minimum at $p_{fx} = 0$ (top left corner of Fig. 7). This minimum indicates that, for an electron along orbit a or b, the probability that the electron reaches the detector with final momentum component $p_{fx} = 0$ is largest.

TABLE II. Behavior of known holographic structures for increasing driving-field ellipticity, together with contributing orbits.

Structure	Interfering orbits	Behavior
fan	a and b	sharper near the p_z axis, blurring for high p_x
spider	b and c	counterclockwise rotation, blurring, prominence in lower half plane
fishbone	a and c	blurring near the p_z axis, contrast retained for high p_x, prominence in upper half plane

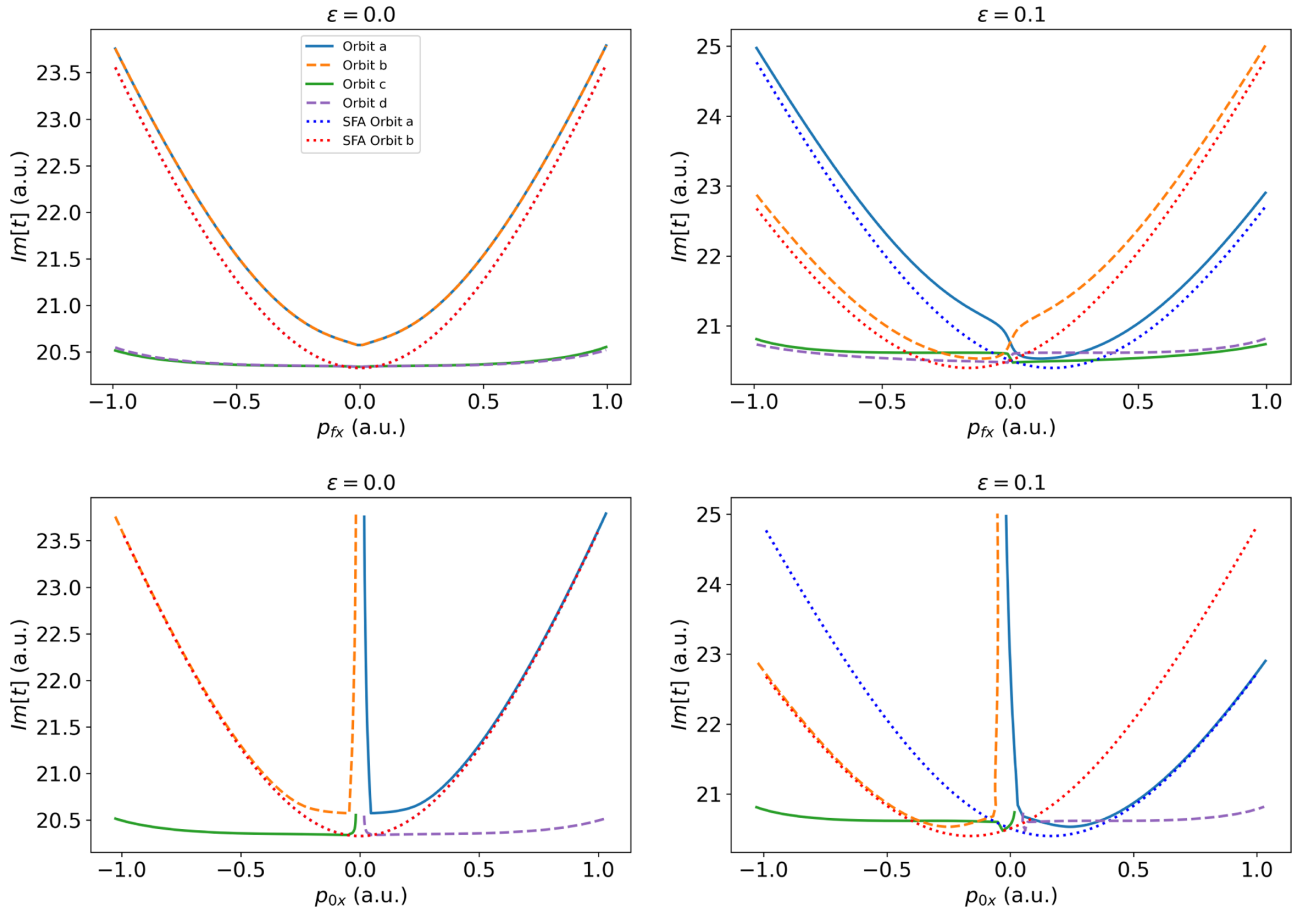

FIG. 7. Imaginary parts of the ionization times t' for the CQSFA and the SFA as functions of the final and initial momentum components p_{fx} and p_{0x} taken along the fixed final p_{fx} axis, with $p_{fz} = 0$ (top and bottom rows, respectively). The calculation was done for helium in a field with an intensity of 2.5×10^{14} W/cm^2 and wavelength of 735 nm. The left and right columns correspond to ellipticities $\epsilon = 0$ and 0.1, respectively. The remaining field and atomic parameters are the same as in the previous figures.

For the SFA, this is related to the effective potential barrier being narrowest, as a nonvanishing p_x will effectively raise the ionization potential (for a discussion of this shift see, e.g., [88]). For the CQSFA, however, the interpretation is subtler, as suggested by $\mathrm{Im}(t')$ plotted against the initial momentum p_{0x} (bottom left corner of Fig. 7). For the CQSFA orbits a and b, the figure shows that $\mathrm{Im}(t') \to \infty$ for $p_{0x} = 0$. This is due to the presence of the Coulomb potential and means that an electron along orbits a and b cannot escape with vanishing perpendicular momenta. This is clear as the Coulomb potential essentially decelerates an electron along orbit a and a field dressed hyperbola starting half a cycle later, namely, orbit b, requires $p_{0x} \neq 0$. Therefore, there will be a minimal escape momentum for the electron, in order for it to reach the detector with final momentum $p_{fx} = 0$. This also holds for the other CQSFA orbits, as the maxima for $\mathrm{Im}(t')$ at $p_{0x} = 0$ indicate. For large absolute values of p_{0x}, the imaginary parts $\mathrm{Im}(t')$ associated with the CQSFA orbits a and b tend to their SFA counterparts. This is expected as, in this limit, they behave as SFA direct orbits and the Coulomb potential does not play a critical role [94]. For the CQSFA orbits c and d the curves are much flatter throughout. This flatter behavior of $\mathrm{Im}(t')$ stems from the real parts of the ionization times being restricted to narrower time ranges, closer to the peak of the field (for a recent discussion for linearly polarized fields see [108]).

Finally, Fig. 7 is also a good indicator of the momentum regions for which the holographic fringes will show high contrast. Similar $\mathrm{Im}(t')$ for different trajectories at a specific final momentum means that their contributions to the whole transition amplitude are comparable, so their interference will exhibit sharp fringes. According to the figure, this would happen for orbits a and b, or orbits c and d for a wide range of perpendicular momenta p_x. An inspection of the PMDs along the $p_z = 0$ axis shows indeed that the fan, caused by the interference orbits a and b, and the carpet, caused by the interference of orbits c and d, exhibit high contrast for the linearly polarized case regardless of p_x. On the other hand, the spider, coming from the interference of orbits b and c, is only expected to be prominent near $p_x = 0$, that is, the field-polarization axis.

This overall behavior changes even for a small ellipticity (see the right column of Fig. 7), for which the $p_x \to -p_x$ reflection symmetry is broken. Nonvanishing ellipticity leads to a tilting of $\mathrm{Im}(t')$ with regard to $p_x = 0$ for orbits a and b, for both the SFA and CQSFA. For all CQSFA orbits, there is a stepwise behavior for $\mathrm{Im}(t')$ around the origin, if plotted as

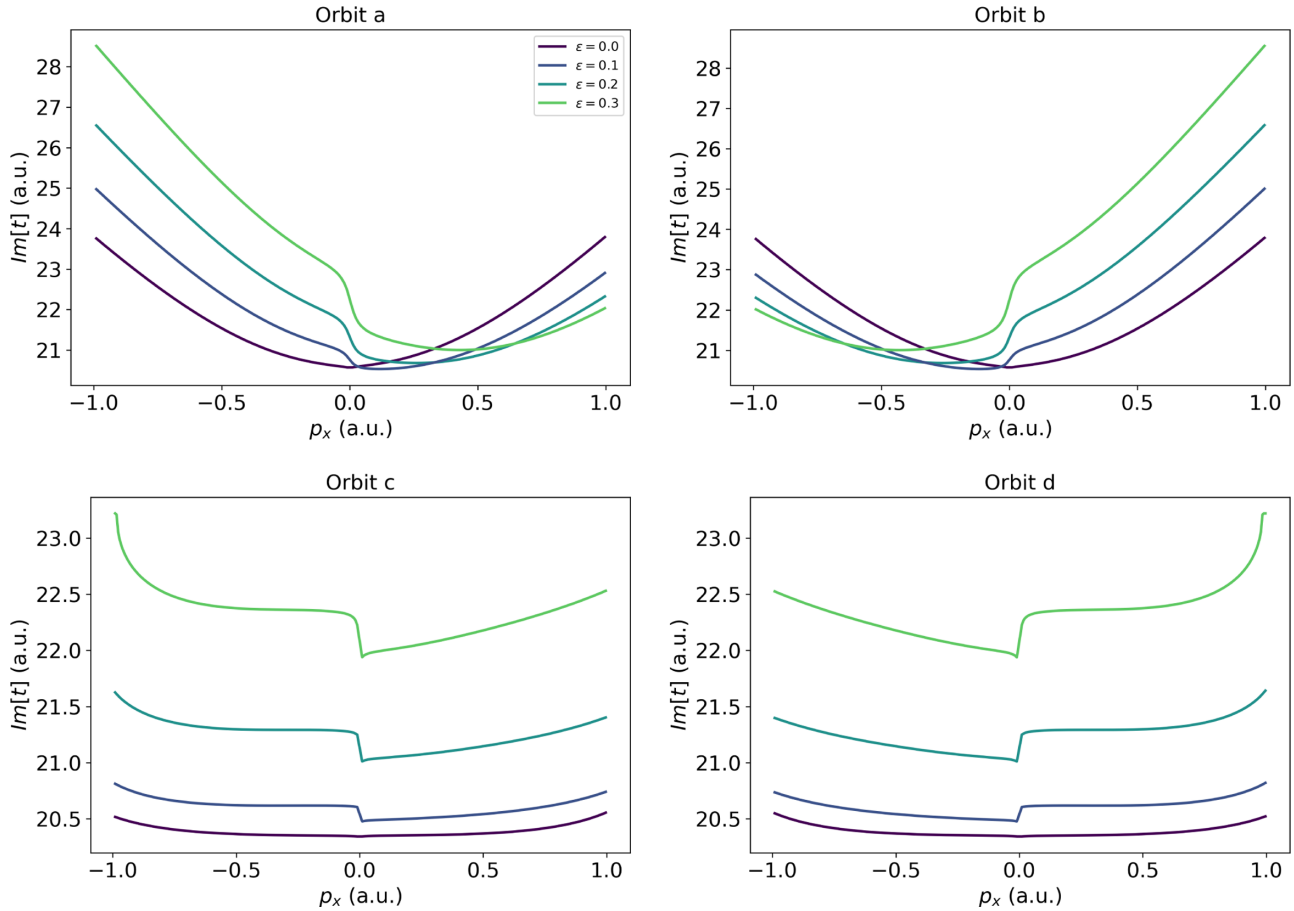

FIG. 8. Imaginary parts of the ionization times t' for the CQSFA orbits a, b, c, and d as functions of the electron's final momentum p_x along the minor polarization axis, for increasing driving-field ellipticities. The orbits are classified according to Sec. III C and the remaining parameters are the same as in the previous figures.

a function of the final momentum p_{fx} (see the top right panel of Fig. 7). This feature is absent for the SFA.

The tilting in $\mathrm{Im}(t')$ is caused by the field components parallel to the minor polarization axis, which either help or hinder the electron ionization along orbits a and b. For instance, for orbit a the tilt to the right indicates that the field component along the minor polarization axis helps ionization for positive momenta, but hinders it for negative momentum. A similar line of reasoning can be used for orbit b tilting to the left, with the difference that in this case the curve will be the mirror image of that observed for orbit a.

The stepwise feature is caused by the Coulomb potential and can be understood by inspecting how $\mathrm{Im}(t')$ behaves as a function of p_{0x} (see the bottom right panel of Fig. 7). Similarly to what happens for linearly polarized field, the electron cannot escape if its perpendicular momentum component p_{0x} is vanishing and there is a minimum momentum value for which it may escape. Nonetheless, due to the field's nonvanishing ellipticity, the escape momenta will be different for the positive and negative momentum half planes. This will lead to the step in $\mathrm{Im}(t')$ near the origin, if plotted as a function of the final momenta p_{fx}. Orbits c and d also exhibit the stepwise behavior mentioned above and for the very same reasons.

An inspection of the top right panel of Fig. 7 also provides valuable insight into the momentum regions for which specific holographic patterns are blurred or sharp. For instance, the structure stemming from interference of orbits a and c becomes sharper away from the major polarization axis because the imaginary parts of the times cross each other for $p_{fx} = 0.5$. This can be confirmed by looking at the corresponding PMD in Fig. 6 (see the right column, second row from the top). Similarly, one expects the spider to be sharper in the lower momentum half plane as $\mathrm{Im}(t')$ for orbits b and c are much closer for $p_{fx} < 0$. The corresponding PMD, located in the second row and middle column in Fig. 6, shows that this is indeed the case.

In Fig. 8 we illustrate more thoroughly how $\mathrm{Im}(t')$ behaves for increasing field ellipticity. We consider the final electron momentum component p_x along the minor polarization axis and plot each CQSFA orbit separately. The tilting for orbits a and b becomes more extreme for increasing ellipticity. This sheds light on the blurring of the fan-shaped fringes, caused by discrepant imaginary parts in the same momentum half plane, and on the shift of the maxima in the PMDs towards larger momentum values, caused by the changes in the minima of $\mathrm{Im}(t')$. For orbits c and d, instead of a tilt, we see a marked increase in $\mathrm{Im}(t')$ with the ellipticity. This hints at both orbits c and d becoming suppressed for larger values of ϵ, which is not surprising, given that these orbits are associated with rescattering and will become rarer in the high-ellipticity regime.

V. CONCLUSIONS

In this work we investigated quantum interference in strong-field ionization in elliptically polarized fields, with emphasis on holographic patterns. We interpreted the features encountered using the Coulomb quantum-orbit strong-field approximation, which was compared to the numerical solution of the time-dependent Schrödinger equation and the standard strong-field approximation, for which the binding potential is absent in the continuum propagation. The CQSFA is an orbit-based method that accounts for tunneling, quantum interference, and the presence of the binding potential in the continuum [94,96,105]. So far, it had only been applied to photoelectron holography in linearly polarized fields. We focus on the low- and intermediate-ellipticity regime, for which intracycle holographic interference is present. This differs from typical studies of photoelectron emission in elliptical fields, whose main objective is to map a single-ionization time to an offset angle. This mapping requires a high ellipticity so that intracycle interference is strongly suppressed [80]. In the low-ellipticity regime, there are many possible ionization times which can be associated with electron orbits.

We find that a nonvanishing ellipticity leads to twists in the holographic patterns. The twists are absent in the plain strong-field approximation, which neglects the residual binding potential, but have been identified in the CQSFA and in TDSE computations. This suggests that they are caused by the interplay of the elliptical field and the central potential. Further support of this is provided by a TDSE computation which truncates the tail of the Coulomb potential, but leaves the effective potential barrier intact. There is a decrease in the twists due to the removal of the Coulomb tail. However, a residual twist is present, which means that there is also a contribution from the barrier. Twists have been observed experimentally in the spider [18] and angular shifts for ATI peaks of increasing order have been reported in [109,110]. However, most studies in the low- to intermediate-ellipticity regime concentrate on Coulomb focusing [111,112], or the maxima and width or the photoelectron momentum distributions [113,114].

As the ellipticity increases, the contrast of the holographic fringes fades and the maxima of the PMDs move further apart. This is due to the transverse components of the momenta upon ionization and during continuum propagation. Estimates for the ellipticity range in which quantum interference is relevant have been provided in this work and agree with the outcomes of the TDSE and CQSFA computations.

The twisting and the blurring are then understood in terms of interfering electron orbits, whose ionization times are first derived analytically in the SFA framework, in a generalization of the expressions in [64,100] to a broader parameter range. These SFA expressions are then used as first guesses for the CQSFA ionization times. A noteworthy issue is that the orbit classification used in the CQSFA is highly dependent on the driving-field shape and existing symmetries. In fact, because the reflection symmetry with regard to the major polarization axis is broken, we have altered the classification in terms of orbits 1–4 [96,103], with regard to the linearly polarized case. Other examples of modified CQSFA orbits have been used in the study of two-color linearly polarized fields [115]. A very useful tool to understand the loss of contrast in the holographic patterns is the imaginary part of the ionization time, which one may relate to the ionization probability associated with a specific type of orbit. Comparable $\mathrm{Im}(t')$ for a pair (i, j) of orbits means that there will be sharp fringes, while $\mathrm{Im}(t_i') \ll \mathrm{Im}(t_j')$ means that blurring will occur. For a specific orbit, nonvanishing ellipticity will break the reflection symmetry of $\mathrm{Im}(t')$ for the lower and upper half planes.

Although the loss of contrast in the holographic patterns is an overall feature, it occurs for different reasons, depending on the types of orbit which create the patterns. If a specific holographic pattern results from the quantum interference of events starting at different half cycles whose momentum components p_x do not change signs, with increasing ellipticity their contributions will mainly populate different half planes. Therefore, their maxima will move further apart and quantum interference will only be significant close to the major polarization axis. This can be observed, for instance, in the fan-shaped fringes. If, on the other hand, the holographic pattern results from events in the same half cycle or p_x changes during propagation, the contribution of such orbits to the PMDs will move to the same momentum half plane. However, those orbits interacting more closely with the core, such as orbits c and d, will become rarer as the ellipticity increases. Consequently, the transition amplitudes associated with those specific pathways will be suppressed and the patterns will blur. This is the case of the spider and of the patterns stemming from the interference of orbits a and c. The widely studied high-ellipticity regime is reached when some of the solutions cease to exist and some merge. Methodologically, this involves Stokes transitions, which, for the field parameters considered in this work, happen outside the parameter range of interest (see Appendixes B and C).

In summary, the twisted patterns reported in this paper are another manifestation of the interplay of the Coulomb potential and the elliptically polarized field: Instead of a single offset angle in the PMD, which can be modeled classically, the long-range potential leads to offsets in holographic patterns, which can be understood in terms of interfering orbits. The present studies may be useful for a wide range of scenarios in which quantum interference is important, such as diatomic molecules in elliptically polarized fields [116].

ACKNOWLEDGMENTS

This work was funded by Grant No. EP/J019143/1, from the UK Engineering and Physical Sciences Research Council. C.H. acknowledges support from a Swiss National Science Foundation mobility fellowship. A.S.M. acknowledges funding from the European Union's Horizon 2020 research and innovation program under the Marie Skłodowska-Curie grant agreement, SSFI No. 887153. G.K. was funded by the University College London (UCL) summer research program sponsored by the World-leading University Fostering Program in Seoul National University and would like to thank UCL for its kind hospitality.

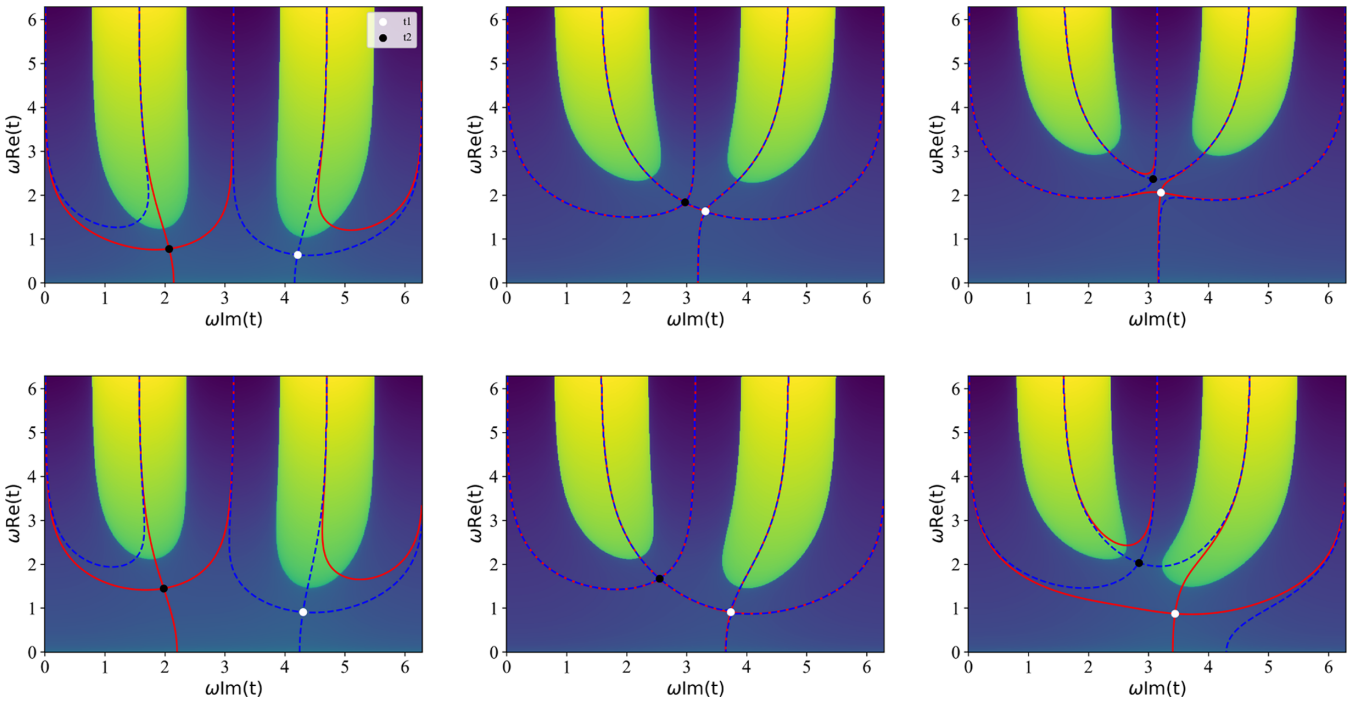

FIG. 9. Contours with the same real part of the action with saddle-point solutions and imaginary part of the action in the background, computed for the SFA. Blue (red) lines are contours with the same real part of the action with the solution t_1 (t_2) and the yellow (blue) background represents the large negative (positive) imaginary part of the action. To calculate the transition amplitude with Eq. (1), the integration should be done along these contours and the integrand is proportional to the $\exp i\,\mathrm{Im}(t)$. Therefore, while calculating the transition amplitude, only the contours which do not pass the yellow area should be selected. The top and bottom panels represent an ellipticity of 0.2 and 0.7, respectively. The left, middle, and right panels represent the perpendicular momentum p_z that is smaller than, the same as, and larger than the critical momentum $p_{z,\mathrm{crit}}$, respectively. From the left panel to the right panel, the topology of the contour changes. This causes the Stokes transition. The remaining field and atomic parameters are the same as in the previous figures.

APPENDIX A: ANALYTIC EXPRESSIONS FOR IONIZATION TIMES

In this Appendix we briefly sketch the procedure to obtain the analytic solutions for the ionization times obtained with the strong-field approximation, which are given in Sec. III. The saddle-point solutions giving the ionization times are obtained from Eq. (21). By substituting $\xi = \cos(\omega t)$ and by replacing $\sin^2(\omega t) = 1 - \xi^2$ in Eq. (21), we can derive a quartic equation for ξ as

$$\xi^4 + 4\bar{p}_z\xi^3 + [2\bar{U} + 4(1+\epsilon^2)\bar{p}_z{}^2]\xi^2 + 4\bar{p}_z\bar{U}\xi + (\bar{U}^2 - 4\bar{p}_x{}^2\epsilon^2) = 0, \tag{A1}$$

where $\bar{p}_z$, $\bar{p}_x$, and $\bar{U}$ are defined as

$$\bar{p}_z = \frac{\sqrt{1+\epsilon^2}}{2(1-\epsilon^2)\sqrt{U_p}}p_z,\ \bar{p}_z = \frac{\sqrt{1+\epsilon^2}}{2(1-\epsilon^2)\sqrt{U_p}}p_z,$$
$$\bar{U} = \frac{1}{(1-\epsilon^2)}\left(\frac{1+\epsilon^2}{4U_p}\left(2I_p + p_z^2 + p_x^2\right) + \epsilon^2\right). \tag{A2}$$

Since the analytic form of the solutions of the quartic equation exists, we can obtain four solutions of the quartic equation as Eq. (29). The explicit form of ζ and η is given as

$$\Delta_0 = A_2^2 - 3A_3A_1 + 12A_0,$$
$$\Delta_1 = 2A_2^3 - 9A_3A_2A_1 + 27A_3^2A_0 + 27A_1^2 - 72A_2A_0,$$
$$Q = \left(\frac{\Delta_1 + i\sqrt{4\Delta_0^3 - \Delta_1^2}}{2}\right)^{1/3},$$
$$\zeta = \frac{1}{2}\sqrt{-\frac{2}{3}(2\bar{U} + 4\epsilon^2\bar{p}_z{}^2 - 2\bar{p}_z{}^2) + \frac{1}{3}\left(Q + \frac{\Delta_0}{Q}\right)},$$
$$\eta = -\frac{8\bar{p}_z{}^3\epsilon^2}{\zeta}, \tag{A3}$$

where A_i are the coefficients of ξ_i in the quartic equation (A1). Note that not all four solutions of the quartic equation are the solution of the original saddle-point equation (21). However, by comparing the sign of Eq. (21), we can find the two valid solution sets as Eq. (29). Furthermore, we have checked that both ζ and η go to zero at zero ellipticity, which makes our solutions consistent with the linearly polarized solution.

APPENDIX B: STOKES TRANSITIONS AND DIVERGENCIES

Within the present formalism, obstacles towards computing PMDs for fields of arbitrary ellipticity are coalescent saddles and Stokes transitions. Coalescent saddles mean that uniform asymptotic expansions that treat them collectively will be required [117]. Stokes transitions lead to the asymptotic expansion becoming inaccurate due to a change of

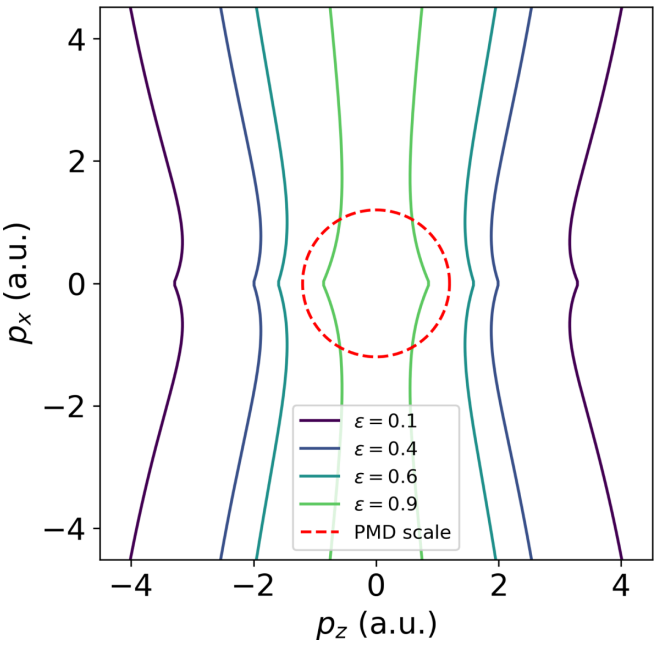

FIG. 10. Critical momenta for different field ellipticities, computed with the SFA. If the perpendicular momentum is larger than the critical momentum indicated by solid lines, a Stokes transition happens. The red dashed circled area shows the relevant momentum range of the PMDs used in this paper. The remaining field and atomic parameters are the same as in the previous figures.

contour. This will result in divergent contributions, which must be discarded (for a detailed discussion and regularization methods see [118]). In this Appendix we will highlight how coalescing saddles and Stokes transitions lead to divergencies in the PMDs and explore in what momentum ranges this happens. This will be illustrated with the SFA. We will go beyond the studies in [64,100], which have been performed along the major polarization axis p_z, and look at how the PMDs are affected as a whole. The CQSFA will present further challenges, such as branch cuts associated with rescattering. Preliminary studies in this direction already exist [95,119], but its full solution is beyond the scope of this article.

In Fig. 9 we illustrate the change in the contour that occurs around a critical value of p_z, called here $p_{z,\mathrm{crit}}$, for which its topology changes. For simplicity, we keep the momentum component p_y parallel to the minor axis fixed. To calculate the transition amplitude we must integrate from $t = -\infty$ to $t = +\infty$ along some contours in the figure, in the upper complex time half plane.[1] Since the action is periodic, it suffices to reduce our problem to a single field cycle. One should note that the contributions from the contours integrating from 0 to $i\infty$ and from $2\pi + i\infty$ to 2π cancel each other.

The blue regions represent areas for which the imaginary part of the action causes the yield to vanish when the imaginary part of ωt tends to infinity, while the green areas depict regions for which it will diverge. The dots illustrate two saddle points, which will lead to key contributions to the PMDs. The contours passing through the saddle points are illustrated by the thick lines in the figure.

For $p_z < p_{z,\mathrm{crit}}$ (left column), the relevant contours encompass the two saddle points. Hence, there are two quantum trajectories engaged in the ionization process, with the saddle S_1 being dominant, as seen from its closeness to the real-time axis. At $p_z = p_{z,\mathrm{crit}}$ (middle column), the real parts of the action associated with saddles S_1 and S_2 become equal, which characterizes a Stokes transition [118]. For $p_z > p_{z,\mathrm{crit}}$ (right column), the contour passing through S_2 will lead to divergencies, so the saddle must be discarded.

Figure 10 displays the critical momenta for different field ellipticities, together with the region for which the PMDs are physically relevant (red dashed circle). This is the scale used in the remaining figures of this article. The figure shows that there is always a Stokes transition. However, the absolute value of $p_{z,\mathrm{crit}}$ decreases for increasing ellipticity. For small and moderate ellipticity, the Stokes transitions occur for momentum ranges far away from the regions of interest and thus can be ignored, while for large ellipticities they encroach more and more into the physically relevant momentum regions. Nonetheless, the Stokes transitions always seem to occur in the half plane opposite to the physically relevant region. Thus, matching the solutions in the physically relevant momentum ranges leads to sickle-shaped distributions, as expected. Including the Coulomb potential will lead to angular offsets, which are absent in the plain SFA (see, for instance, Figs. 2–4 in the main text).

APPENDIX C: CIRCULAR POLARIZATION LIMIT FOR IONIZATION TIME

For circularly polarized fields, there will be a single-ionization time, which can be associated with a specific angle in the PMDs. This is the key idea upon which the attosecond angular streaking, also known as the attoclock, is based. Below we show how this time can be inferred analytically, using the SFA solution for the tunnel ionization time.

For circular polarization ($\epsilon = 1$), the saddle-point equation for t' becomes

$$(p_z + \sqrt{2U_p}\cos\omega t')^2 + (p_x + \sqrt{2U_p}\sin\omega t')^2 = -2I_p. \tag{C1}$$

This is the equation of a circle with complex radius centered at

$$(p_x, p_z) = (-\sqrt{2U_p}\sin\omega t', -\sqrt{2U_p}\cos\omega t'), \tag{C2}$$

which will lead to a ring-shaped distribution, due to the rotational symmetry. One may also show that, in this limit, $\mathrm{Re}(t')$ will be step functions. Thus, for each angle, the electron will escape at the time for which the field will have an extremum. The step happens when switching to different momentum half planes.

Below we show that this holds for specific angles, but due to the symmetry of the problem this can be extended to an arbitrary axis using a rotation matrix. If we choose a momentum along the p_z axis ($p_x = 0$), Eq. (C1) becomes

$$p_z^2 + 2U_p + 2p_z\sqrt{U_p}\cos\omega t' = -2I_p \tag{C3}$$

[1]The lower half plane would lead to unphysical results associated with diverging contributions inside a potential barrier [95,119]; for a review on saddle-point methods in strong fields see [120].

so that

$$\cos\omega t' = \frac{-1}{p_z\sqrt{2U_p}}\left[I_p + U_p + \frac{p_z^2}{2}\right]. \tag{C4}$$

Setting $t' = t'_r + it'_i$ in Eq. (C4) gives

$$\cos\omega t'_r \cosh\omega t'_i = \frac{-1}{p_z\sqrt{2U_p}}\left[I_p + U_p + \frac{p_z^2}{2}\right] \tag{C5}$$

and

$$\sin\omega t'_r \sinh\omega t'_i = 0. \tag{C6}$$

Since t'_i cannot vanish because tunneling is classically forbidden, $\sin\omega t'_r = 0$, which means that $\omega t'_r = n\pi$. Similarly, along the p_x axis we find

$$\sin\omega t' = \frac{-1}{p_x\sqrt{2U_p}}\left[I_p + U_p + \frac{p_x^2}{2}\right], \tag{C7}$$

so

$$\omega t'_r = \frac{(2n+1)\pi}{2}, \tag{C8}$$

which corresponds to an extremum for the other component of the field.

[1] P. Agostini, F. Fabre, G. Mainfray, G. Petite, and N. K. Rahman, Phys. Rev. Lett. **42**, 1127 (1979).
[2] W. Becker, F. Grasbon, R. Kopold, D. B. Milošević, G. G. Paulus, and H. Walther, Adv. At. Mol. Opt. Phys. **48**, 35 (2002).
[3] D. B. Milošević, G. G. Paulus, D. Bauer, and W. Becker, J. Phys. B **39**, R203 (2006).
[4] P. B. Corkum, Phys. Rev. Lett. **71**, 1994 (1993).
[5] M. Lein, J. Phys. B **40**, R135 (2007).
[6] F. Krausz and M. Ivanov, Rev. Mod. Phys. **81**, 163 (2009).
[7] P. Salières, A. Maquet, S. Haessler, J. Caillat, and R. Taïeb, Rep. Prog. Phys. **75**, 062401 (2012).
[8] L. Gallmann, C. Cirelli, and U. Keller, Annu. Rev. Phys. Chem. **63**, 447 (2012).
[9] F. Lépine, M. Y. Ivanov, and M. J. J. Vrakking, Nat. Photon. **8**, 195 (2014).
[10] Y. Huismans, A. Rouzée, A. Gijsbertsen, J. H. Jungmann, A. S. Smolkowska, P. S. W. M. Logman, F. Lépine, C. Cauchy, S. Zamith, T. Marchenko *et al.*, Science **331**, 61 (2011).
[11] X.-B. Bian, Y. Huismans, O. Smirnova, K.-J. Yuan, M. J. J. Vrakking, and A. D. Bandrauk, Phys. Rev. A **84**, 043420 (2011).
[12] X.-B. Bian and A. D. Bandrauk, Phys. Rev. Lett. **108**, 263003 (2012).
[13] C. F. d. M. Faria and A. S. Maxwell, Rep. Prog. Phys. **83**, 034401 (2020).
[14] X. Xie, Phys. Rev. Lett. **114**, 173003 (2015).
[15] X. Gong, C. Lin, F. He, Q. Song, K. Lin, Q. Ji, W. Zhang, J. Ma, P. Lu, Y. Liu *et al.*, Phys. Rev. Lett. **118**, 143203 (2017).
[16] M. Han, P. Ge, Y. Shao, M.-M. Liu, Y. Deng, C. Wu, Q. Gong, and Y. Liu, Phys. Rev. Lett. **119**, 073201 (2017).
[17] M. Han, P. Ge, Y. Shao, Q. Gong, and Y. Liu, Phys. Rev. Lett. **120**, 073202 (2018).
[18] H. Xie, M. Li, S. Luo, Y. Li, J. Tan, Y. Zhou, W. Cao, and P. Lu, Opt. Lett. **43**, 3220 (2018).
[19] T. Brabec and F. Krausz, Rev. Mod. Phys. **72**, 545 (2000).
[20] F. Ehlotzky, Phys. Rep. **345**, 175 (2001).
[21] D. Shafir, H. Soifer, B. D. Bruner, M. Dagan, Y. Mairesse, S. Patchkovskii, M. Y. Ivanov, O. Smirnova, and N. Dudovich, Nature (London) **485**, 343 (2012).
[22] M. Richter, M. Kunitski, M. Schöffler, T. Jahnke, L. P. Schmidt, M. Li, Y. Liu, and R. Dörner, J. Phys.: Conf. Ser. **635**, 092036 (2015).
[23] T. Das, B. B. Augstein, C. Figueira de Morisson Faria, L. E. Chipperfield, D. J. Hoffmann, and J. P. Marangos, Phys. Rev. A **92**, 023406 (2015).
[24] J. Henkel and M. Lein, Phys. Rev. A **92**, 013422 (2015).
[25] Y. Li, Y. Zhou, M. He, M. Li, and P. Lu, Opt. Express **24**, 23697 (2016).
[26] L. Zhang, X. Xie, S. Roither, D. Kartashov, Y. Wang, C. Wang, M. Schöffler, D. Shafir, P. B. Corkum, A. Baltuška, I. Ivanov, A. Kheifets, X. Liu, A. Staudte, and M. Kitzler, Phys. Rev. A **90**, 061401(R) (2014).
[27] X. Xie, T. Wang, S. Yu, X. Lai, S. Roither, D. Kartashov, A. Baltuška, X. Liu, A. Staudte, and M. Kitzler, Phys. Rev. Lett. **119**, 243201 (2017).
[28] V. A. Tulsky, M. A. Almajid, and D. Bauer, Phys. Rev. A **98**, 053433 (2018).
[29] D. B. Milošević, W. Becker, and R. Kopold, Phys. Rev. A **61**, 063403 (2000).
[30] O. Smirnova, Y. Mairesse, and S. Patchkovskii, J. Phys. B **48**, 234005 (2015).
[31] D. B. Milošević, Phys. Rev. A **92**, 043827 (2015).
[32] D. B. Milošević and W. Becker, Phys. Rev. A **93**, 063418 (2016).
[33] C. A. Mancuso, D. D. Hickstein, K. M. Dorney, J. L. Ellis, E. Hasović, R. Knut, P. Grychtol, C. Gentry, M. Gopalakrishnan, D. Zusin *et al.*, Phys. Rev. A **93**, 053406 (2016).
[34] V.-H. Hoang, V.-H. Le, C. D. Lin, and A.-T. Le, Phys. Rev. A **95**, 031402(R) (2017).
[35] M. A. Almajid, M. Zabel, S. Skruszewicz, J. Tiggesbäumker, and D. Bauer, J. Phys. B **50**, 194001 (2017).
[36] M. Busuladžić, A. Gazibegović-Busuladžić, and D. B. Milošević, Phys. Rev. A **95**, 033411 (2017).
[37] S. Eckart, M. Kunitski, I. Ivanov, M. Richter, K. Fehre, A. Hartung, J. Rist, K. Henrichs, D. Trabert, N. Schlott, L. P. H. Schmidt, T. Jahnke, M. S. Schöffler, A. Kheifets, and R. Dörner, Phys. Rev. A **97**, 041402(R) (2018).
[38] D. B. Milošević and W. Becker, J. Phys. B **51**, 054001 (2018).
[39] D. Ayuso, P. Decleva, S. Patchkovskii, and O. Smirnova, J. Phys. B **51**, 06LT01 (2018).
[40] D. Ayuso, P. Decleva, S. Patchkovskii, and O. Smirnova, J. Phys. B **51**, 124002 (2018).
[41] D. Baykusheva and H. J. Wörner, Phys. Rev. X **8**, 031060 (2018).
[42] N. Eicke and M. Lein, Phys. Rev. A **99**, 031402(R) (2019).

[43] S. Yue, S. Brennecke, H. Du, and M. Lein, Phys. Rev. A **101**, 053438 (2020).

[44] A. S. Maxwell, G. S. J. Armstrong, M. F. Ciappina, E. Pisanty, Y. Kang, A. C. Brown, M. Lewenstein, and C. Figueira de Morisson Faria, Faraday Discuss. **228**, 394 (2021).

[45] N. Dudovich, O. Smirnova, J. Levesque, Y. Mairesse, M. Y. Ivanov, D. M. Villeneuve, and P. B. Corkum, Nat. Phys. **2**, 781 (2006).

[46] X. Xie, S. Roither, S. Gräfe, D. Kartashov, E. Persson, C. Lemell, L. Zhang, M. S. Schöffler, A. Baltuška, J. Burgdörfer *et al.*, New J. Phys. **15**, 043050 (2013).

[47] D. G. Arbó, S. Nagele, X.-M. Tong, X. Xie, M. Kitzler, and J. Burgdörfer, Phys. Rev. A **89**, 043414 (2014).

[48] S. Skruszewicz, J. Tiggesbäumker, K.-H. Meiwes-Broer, M. Arbeiter, T. Fennel, and D. Bauer, Phys. Rev. Lett. **115**, 043001 (2015).

[49] X. Xie, S. Roither, D. Kartashov, L. Zhang, A. Baltuška, and M. Kitzler, High Power Laser Sci. Eng. **4**, e40 (2016).

[50] S. Luo, M. Li, H. Xie, P. Zhang, S. Xu, Y. Li, Y. Zhou, P. Lan, and P. Lu, Phys. Rev. A **96**, 023417 (2017).

[51] G. Porat, G. Alon, S. Rozen, O. Pedatzur, M. Krüger, D. Azoury, A. Natan, G. Orenstein, B. D. Bruner, M. J. J. Vrakking *et al.*, Nat. Commun. **9**, 2805 (2018).

[52] T. Nubbemeyer, K. Gorling, A. Saenz, U. Eichmann, and W. Sandner, Phys. Rev. Lett. **101**, 233001 (2008).

[53] M. Abu-samha and L. B. Madsen, Phys. Rev. A **84**, 023411 (2011).

[54] T. Das, B. B. Augstein, and C. Figueira de Morisson Faria, Phys. Rev. A **88**, 023404 (2013).

[55] C. Hofmann, T. Zimmermann, A. Zielinski, and A. S. Landsman, New J. Phys. **18**, 043011 (2016).

[56] J. Daněk, M. Klaiber, K. Z. Hatsagortsyan, C. H. Keitel, B. Willenberg, J. Maurer, B. W. Mayer, C. R. Phillips, L. Gallmann, and U. Keller, J. Phys. B **51**, 114001 (2018).

[57] I. A. Ivanov and A. S. Kheifets, Phys. Rev. A **89**, 021402(R) (2014).

[58] L. Torlina, F. Morales, J. Kaushal, I. Ivanov, A. Kheifets, A. Zielinski, A. Scrinzi, H. G. Muller, S. Sukiasyan, M. Ivanov, and O. Smirnova, Nat. Phys. **11**, 503 (2015).

[59] N. Eicke and M. Lein, Phys. Rev. A **97**, 031402(R) (2018).

[60] U. S. Sainadh, H. Xu, X. Wang, A. Atia-Tul-Noor, W. C. Wallace, N. Douguet, A. Bray, I. Ivanov, K. Bartschat, A. Kheifets *et al.*, Nature (London) **568**, 75 (2019).

[61] K. C. Kulander, K. J. Schafer, and J. L. Krause, in *Super-Intense Laser-Atom Physics*, edited by B. Piraux, A. L'Huillier, and K. Rzążewski (Springer US, New York, 1993), pp. 95–110.

[62] A. N. Pfeiffer, C. Cirelli, M. Smolarski, D. Dimitrovski, M. Abu-samha, L. B. Madsen, and U. Keller, Nat. Phys. **8**, 76 (2012).

[63] A. S. Landsman, M. Weger, J. Maurer, R. Boge, A. Ludwig, S. Heuser, C. Cirelli, L. Gallmann, and U. Keller, Optica **1**, 343 (2014).

[64] G. G. Paulus, F. Zacher, H. Walther, A. Lohr, W. Becker, and M. Kleber, Phys. Rev. Lett. **80**, 484 (1998).

[65] L. Torlina, J. Kaushal, and O. Smirnova, Phys. Rev. A **88**, 053403 (2013).

[66] S. V. Popruzhenko, J. Phys. B **47**, 204001 (2014).

[67] K. Amini, J. Biegert, F. Calegari, A. Chacón, M. F. Ciappina, A. Dauphin, D. K. Efimov, C. F. d. M. Faria, K. Giergiel, P. Gniewek *et al.*, Rep. Prog. Phys. **82**, 116001 (2019).

[68] A. Rudenko, K. Zrost, C. D. Schröter, V. L. B. de Jesus, B. Feuerstein, R. Moshammer, and J. Ullrich, J. Phys. B **37**, L407 (2004).

[69] C. M. Maharjan, A. S. Alnaser, I. Litvinyuk, P. Ranitovic, and C. L. Cocke, J. Phys. B **39**, 1955 (2006).

[70] R. Gopal, K. Simeonidis, R. Moshammer, T. Ergler, M. Dürr, M. Kurka, K.-U. Kühnel, S. Tschuch, C.-D. Schröter, D. Bauer *et al.*, Phys. Rev. Lett. **103**, 053001 (2009).

[71] Y. Huismans, A. Gijsbertsen, A. S. Smolkowska, J. H. Jungmann, A. Rouzée, P. S. W. M. Logman, F. Lépine, C. Cauchy, S. Zamith, T. Marchenko *et al.*, Phys. Rev. Lett. **109**, 013002 (2012).

[72] T. Marchenko, Y. Huismans, K. J. Schafer, and M. J. J. Vrakking, Phys. Rev. A **84**, 053427 (2011).

[73] D. D. Hickstein, P. Ranitovic, S. Witte, X.-M. Tong, Y. Huismans, P. Arpin, X. Zhou, K. E. Keister, C. W. Hogle, B. Zhang *et al.*, Phys. Rev. Lett. **109**, 073004 (2012).

[74] A. S. Maxwell, C. F. d. M. Faria, X. Lai, R. Sun, and X. Liu, Phys. Rev. A **102**, 033111 (2020).

[75] P. Qin, X. Sun, Y. Liu, and Z. Chen, Phys. Rev. A **104**, 053111 (2021).

[76] N. Werby, A. S. Maxwell, R. Forbes, P. H. Bucksbaum, and C. F. d. M. Faria, Phys. Rev. A **104**, 013109 (2021).

[77] H. Kang, A. S. Maxwell, D. Trabert, X. Lai, S. Eckart, M. Kunitski, M. Schöffler, T. Jahnke, X. Bian, R. Dörner, and C. F. d. M. Faria, Phys. Rev. A **102**, 013109 (2020).

[78] H. Reiss, Phys. Rev. Lett. **101**, 043002 (2008).

[79] A. S. Landsman and U. Keller, Phys. Rep. **547**, 1 (2015).

[80] C. Hofmann, A. S. Landsman, and U. Keller, J. Mod. Opt. **66**, 1052 (2019).

[81] A. Emmanouilidou, A. Chen, C. Hofmann, U. Keller, and A. S. Landsman, J. Phys. B **48**, 245602 (2015).

[82] V. P. Majety and A. Scrinzi, J. Mod. Opt. **64**, 1026 (2017).

[83] V. Tulsky and D. Bauer, Comput. Phys. Commun. **251**, 107098 (2020).

[84] X. M. Tong and C. D. Lin, J. Phys. B: At. Mol. Opt. Phys. **38**, 2593 (2005).

[85] S. P. Goreslavski, G. G. Paulus, S. V. Popruzhenko, and N. I. Shvetsov-Shilovski, Phys. Rev. Lett. **93**, 233002 (2004).

[86] C. F. d. M. Faria, R. Kopold, W. Becker, and J. M. Rost, Phys. Rev. A **65**, 023404 (2002).

[87] J. Wu, B. B. Augstein, and C. Figueira de Morisson Faria, Phys. Rev. A **88**, 023415 (2013).

[88] T. Shaaran, M. T. Nygren, and C. Figueira de Morisson Faria, Phys. Rev. A **81**, 063413 (2010).

[89] T. Shaaran and C. F. d. M. Faria, J. Mod. Opt. **57**, 984 (2010).

[90] L. V. Keldysh, Sov. Phys. JETP **20**, 1307 (1965) [J. Exptl. Theoret. Phys. (U.S.S.R.) **47**, 1945 (1964)].

[91] F. H. M. Faisal, J. Phys. B **6**, L89 (1973).

[92] H. R. Reiss, Phys. Rev. A **22**, 1786 (1980).

[93] A. Lohr, M. Kleber, R. Kopold, and W. Becker, Phys. Rev. A **55**, R4003 (1997).

[94] A. S. Maxwell, A. Al-Jawahiry, T. Das, and C. F. d. M. Faria, Phys. Rev. A **96**, 023420 (2017).

[95] A. S. Maxwell, S. V. Popruzhenko, and C. F. d. M. Faria, Phys. Rev. A **98**, 063423 (2018).

[96] X.-Y. Lai, C. Poli, H. Schomerus, and C. F. d. M. Faria, Phys. Rev. A **92**, 043407 (2015).
[97] S. Brennecke, N. Eicke, and M. Lein, Phys. Rev. Lett. **124**, 153202 (2020).
[98] M. V. Ammosov, N. B. Delone, and V. P. Krainov, Sov. Phys. JETP **64**, 1191 (1986) [Zh. Eksp. Teor. Fiz. **91**, 2008 (1986)].
[99] N. B. Delone and V. P. Krainov, J. Opt. Soc. Am. B **8**, 1207 (1991).
[100] A. Jašarević, E. Hasović, R. Kopold, W. Becker, and D. Milošević, J. Phys. A: Math. Theor. **53**, 125201 (2020).
[101] P. Eckle, M. Smolarski, P. Schlup, J. Biegert, A. Staudte, M. Schöffler, H. G. Muller, R. Dörner, and U. Keller, Nat. Phys. **4**, 565 (2008).
[102] P. Eckle, A. N. Pfeiffer, C. Cirelli, A. Staudte, R. Dörner, H. G. Muller, M. Büttiker, and U. Keller, Science **322**, 1525 (2008).
[103] T.-M. Yan, S. V. Popruzhenko, M. J. J. Vrakking, and D. Bauer, Phys. Rev. Lett. **105**, 253002 (2010).
[104] V. Mosert and D. Bauer, Comput. Phys. Commun. **207**, 452 (2016).
[105] X. Lai, S. Yu, Y. Huang, L. Hua, C. Gong, W. Quan, C. F. d. M. Faria, and X. Liu, Phys. Rev. A **96**, 013414 (2017).
[106] N. Camus, E. Yakaboylu, L. Fechner, M. Klaiber, M. Laux, Y. Mi, K. Z. Hatsagortsyan, T. Pfeifer, C. H. Keitel, and R. Moshammer, Phys. Rev. Lett. **119**, 023201 (2017).
[107] A. Khan, D. Trabert, S. Eckart, M. Kunitski, T. Jahnke, and R. Dörner, Phys. Rev. A **101**, 023409 (2020).
[108] N. Werby, A. S. Maxwell, R. Forbes, C. F. d. M. Faria, and P. H. Bucksbaum, Time correlation filtering reveals two-path electron quantum interference in strong-field ionization, Phys. Rev. A **106**, 033118 (2022).
[109] D. Trabert, N. Anders, S. Brennecke, M. S. Schöffler, T. Jahnke, L. P. H. Schmidt, M. Kunitski, M. Lein, R. Dörner, and S. Eckart, Phys. Rev. Lett. **127**, 273201 (2021).
[110] Z. Xiao, W. Quan, S. Yu, X. Lai, X. Liu, Z. Wei, and J. Chen, Opt. Express **30**, 14873 (2022).
[111] D. Shafir, H. Soifer, C. Vozzi, A. S. Johnson, A. Hartung, Z. Dube, D. M. Villeneuve, P. B. Corkum, N. Dudovich, and A. Staudte, Phys. Rev. Lett. **111**, 023005 (2013).
[112] M. Li, Y. Liu, H. Liu, Q. Ning, L. Fu, J. Liu, Y. Deng, C. Wu, L.-Y. Peng, and Q. Gong, Phys. Rev. Lett. **111**, 023006 (2013).
[113] J.-W. Geng, L. Qin, M. Li, W.-H. Xiong, Y. Liu, Q. Gong, and L.-Y. Peng, J. Phys. B **47**, 204027 (2014).
[114] M. Han, M. Li, M.-M. Liu, and Y. Liu, Phys. Rev. A **95**, 023406 (2017).
[115] T. Rook and C. F. d. M. Faria, J. Phys. B At. Mol. Opt. Phys. **55**, 165601 (2022).
[116] W. Yang, Z. Sheng, X. Feng, M. Wu, Z. Chen, and X. Song, Opt. Express **22**, 2519 (2014).
[117] C. Figueira de Morisson Faria, H. Schomerus, and W. Becker, Phys. Rev. A **66**, 043413 (2002).
[118] M. V. Berry, Proc. R. Soc. London Ser. A **422**, 7 (1989).
[119] E. Pisanty and M. Ivanov, Phys. Rev. A **93**, 043408 (2016).
[120] A. Nayak, M. Dumergue, S. Kühn, S. Mondal, T. Csizmadia, N. Harshitha, M. Füle, M. U. Kahaly, B. Farkas, B. Major *et al.*, Phys. Rep. **833**, 1 (2019).